Nationaal Lucht- en Ruimtevaartlaboratorium
National Aerospace Laboratory NLR

Executive Summary

Micro-mechanical constitutive model for a nickel-base superalloy

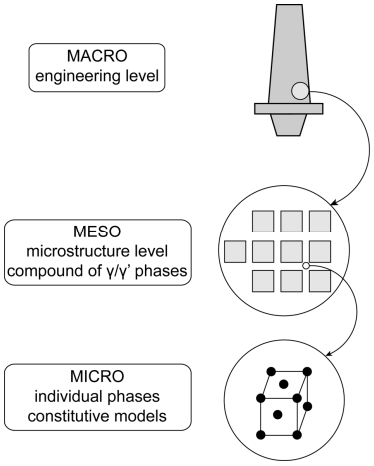

Overview of multi-scale approach

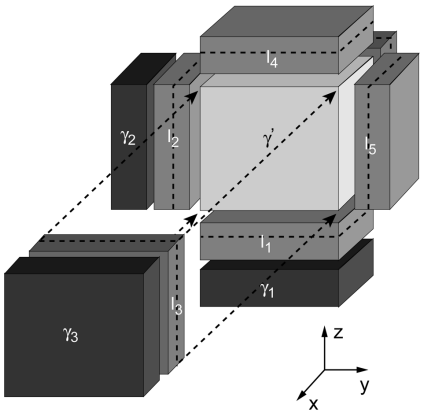

Microstructural unit cell

Problem area
Single crystal nickel-base super-alloys are widely used as gas turbine blade materials because of their high resistance against high temperature inelastic deformation. The superior high temperature behaviour is attributed to the two-phase composite microstructure consisting of a γ-matrix containing a large volume fraction of γ'-particles.
The ability to perform a reliable life time assessment is crucial for both gas turbine component design and maintenance. However, most of the available material models only consider plastic deformation of the matrix phase and neglect precipitate plastic deformation.

Description of work
A recently proposed micro-mechanical model for a Ni-base superalloy has been extended with a precipitate phase constitutive model. Two precipitate deformation mechanisms, precipitate shearing and recovery climb, are included in the model. Dislocation density based formulations are derived to describe their effect on the material mechanical behaviour. Furthermore, the typical anomalous yield behaviour of Ni_3Al intermetallics is implemented in the framework. A database of experimental results on the commercial alloy CMSX-4 is used to determine the model parameters.

Report no.
NLR-TP-2006-641

Authors
T. Tinga
W.A.M. Brekelmans
M.G.D. Geers

Classification report
Unclassified

Date
November 2006

Knowledge Areas
Levensduurbewaking en onderhoud van vliegtuigen
Gasturbine-technologie
Computational Mechanics & Simulation Technology

Descriptors
Constitutive model
Finite Element method
Ni-base superalloys

This report is based on an article submitted to the Journal of the Mechanics and Physics of Solids, by Elsevier Science.

Results and conclusions
It is shown that the material tensile response and creep behaviour for this alloy can be predicted for a range of temperatures, stress and strain rate levels. Also, the effects of the precipitate anomalous yield behaviour and other non-Schmid effects on the superalloy mechanical response are demonstrated.

Applicability
The presented model can be used to simulate superalloy mechanical behaviour for different microstructural dimensions and for a range of different operating conditions.

Nationaal Lucht- en Ruimtevaartlaboratorium, National Aerospace Laboratory NLR

Anthony Fokkerweg 2, 1059 CM Amsterdam,
P.O. Box 90502, 1006 BM Amsterdam, The Netherlands
Telephone +31 20 511 31 13, Fax +31 20 511 32 10, Web site: www.nlr.nl

Nationaal Lucht- en Ruimtevaartlaboratorium
National Aerospace Laboratory NLR

NLR-TP-2006-641

Micro-mechanical constitutive model for a nickel-base superalloy

T. Tinga, W.A.M. Brekelmans[1] and M.G.D. Geers[1]

[1] Technische Universiteit Eindhoven

This report is based on an article submitted to the Journal of the Mechanics and Physics of Solids, by Elsevier Science.

The contents of this report may be cited on condition that full credit is given to NLR and the authors.
This publication has been refereed by the Advisory Committee AEROSPACE VEHICLES.

Customer	National Aerospace Laboratory NLR
Contract number	----
Owner	National Aerospace Laboratory NLR
Division	Aerospace Vehicles
Distribution	Unlimited
Classification of title	Unclassified
	November 2006

Approved by:

Author	Reviewer	Managing department
13/11	13/11	17/11

Summary

This report contains a paper that was submitted to the Journal of the Mechanics and Physics of Solids, by Elsevier Science. The abstract of the paper is given below.

A recently proposed crystal plasticity framework for single crystal Ni-based superalloys is extended with a precipitate phase constitutive model. Two precipitate deformation mechanisms, precipitate shearing and recovery climb, are discussed in detail and dislocation density based formulations are derived to describe their effect on the material mechanical behaviour. Furthermore, the typical anomalous yield behaviour of Ni_3Al intermetallics is discussed and implemented in the framework. A database of experimental results on the commercial alloy CMSX-4 is used to determine the model parameters. It is shown that the material tensile response and creep behaviour for this alloy can be predicted for a range of temperatures, stress and strain rate levels.

Contents

1 Introduction **5**

2 Multi-scale framework **9**

3 Crystal plasticity and internal stresses **12**

3.1 Strain-gradient crystal plasticity 12

3.2 Internal stresses 13

4 Constitutive models **15**

4.1 Matrix phase 15

4.2 Precipitate phase 17

4.2.1 Precipitate deformation mechanisms 17

4.2.2 Crystal plasticity formulation for particle shearing 21

4.2.3 Crystal plasticity formulation for climb 25

4.2.4 Total precipitate deformation 27

5 Model parameter determination **27**

6 Results **31**

6.1 Simulation of creep and tensile tests 31

6.2 Micro-level results 33

6.3 Anomalous yield behaviour 35

7 Conclusions **37**

References **37**

Micro-mechanical constitutive model for a nickel-base superalloy

T. Tinga[*], W.A.M. Brekelmans[$], M.G.D. Geers[$]

[*] *National Aerospace Laboratory NLR, Anthony Fokkerweg 2, 1059 CM, Amsterdam, The Netherlands*

[$] *Eindhoven University of Technology, Department of Mechanical Engineering, P.O. Box 513, 5600 MB Eindhoven, The Netherlands*

Abstract

A recently proposed crystal plasticity framework for single crystal Ni-based superalloys is extended with a precipitate phase constitutive model. Two precipitate deformation mechanisms, precipitate shearing and recovery climb, are discussed in detail and dislocation density based formulations are derived to describe their effect on the material mechanical behaviour. Furthermore, the typical anomalous yield behaviour of Ni_3Al intermetallics is discussed and implemented in the framework. A database of experimental results on the commercial alloy CMSX-4 is used to determine the model parameters. It is shown that the material tensile response and creep behaviour for this alloy can be predicted for a range of temperatures, stress and strain rate levels.

Keywords: A. dislocations; A. microstructures; A. strengthening and mechanisms; B. constitutive behaviour; B. crystal plasticity.

1 Introduction

The superior high temperature behaviour of single crystal nickel-based superalloys is attributed to their characteristic two-phase composite microstructure. This microstructure consists of a γ-matrix containing a large volume fraction of γ'-particles (see Figure 1). The Ni_3Al (γ') -precipitates are cuboidal and are more or less regularly distributed in a Ni-matrix (γ-phase). The typical precipitate size is 0.5 μm and the matrix channel width is typically 60 nm. The material's high resistance against inelastic deformation at elevated temperatures makes it very suitable for use as gas turbine blade material.

[*] Corresponding author. Tel.: +31-527-248727; fax: +31-527-248210.
Email address: tinga@nlr.nl

The design process of gas turbine components, but also the maintenance and overhaul activities, require a reliable prediction of the thermo-mechanical deformation of the used materials. Therefore, modelling of the mechanical behaviour of superalloys has been subject of numerous studies. Initially the material was treated as a homogeneous single phase material (Ghosh et al., 1990; Hanriot et al., 1991; Jordan et al., 1993; Yue et al., 1996; Pan et al., 1997; Yue and Lu, 1998; Busso et al., 2000b; Rist et al., 2000; MacLachlan et al., 2002; Daniel et al., 2002; Cailletaud et al., 2003; Shenoy et al., 2005). Since these solution approaches are addressing the macroscopic level, they can easily be used as a constitutive description in a finite element (FE) analysis, which is nowadays the common method used for component stress analysis and life time assessment.

More recently, models were developed that take into account the two-phase nature of superalloys. In these microstructural models the shape, dimensions and properties of both phases are considered as model parameters. However, the length scale of the microstructure, which is in the order of micrometers, is much smaller than the engineering length scale. Modelling an entire macroscopic component taking into account all microstructural details is therefore not feasible in the engineering practice.

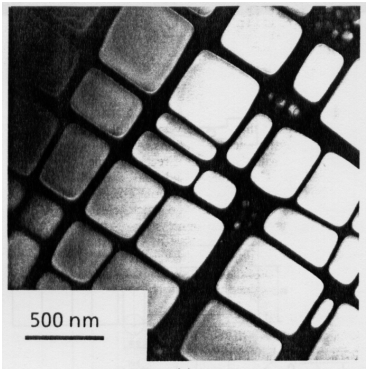

Figure 1 Micrograph of a superalloy microstructure showing the cuboidal γ'-precipitates in a γ-matrix (Moss et al., 1996).

On the one hand, this difference in length scales can be covered by using a multi-scale approach in which an appropriate homogenization method is applied to connect the microscopic to the macroscopic level. A large number of multi-scale frameworks have been developed in the past decades for different materials (Eshelby, 1957; Bensoussan et al., 1978; Sanchez-Palencia, 1980; Willis, 1981; Ponte Castañeda and Suquet, 1998; Michel et al., 1999; Miehe et al., 1999; Kouznetsova et al., 2002; Evers et al., 2002). Among these, Fedelich (1999, 2002) developed a model to describe the mechanical behaviour of Ni-based superalloys. The constitutive behaviour of the two phases was derived from the underlying dislocation based deformation mechanisms in the material.

On the other hand, the length scale problem can be overcome by using microstructural models that predict the material response in a closed-form set of equations on the level of a material point (Busso and McClintock, 1996; Svoboda and Lukas, 1997; Kuttner and Wahi, 1998; Busso et al., 2000a; Svoboda and Lukas, 2000; Meissonnier et al., 2001; Choi et al., 2005). The microstructural results are then used to develop constitutive descriptions that fit in traditional methods at the macroscopic level. Busso and co-workers (Busso and McClintock, 1996; Busso et al., 2000a; Meissonnier et al., 2001) constructed a detailed unit cell FE model of an elastic γ'-precipitate embedded in an elasto-viscoplastic γ-matrix. Choi et al. (2005) extended this work using a more phenomenological crystal plasticity formulation.

All the microstructural models mentioned above are based on a unit cell approach, in which a characteristic volume is defined that contains both γ- and γ'-phase material with their respective properties and dimensions. However, almost all models treat the precipitate phase as an elastic medium in which no plastic deformation occurs. Only Fedelich (1999, 2002) and Svoboda and Lukas (1997, 2000) developed models for Ni-based superalloys that include inelastic deformation of the precipitate.

On the other hand, a lot of experimental research (Pollock and Argon, 1994; Sass and Feller-Kniepmeier, 1998; Svoboda and Lukas, 2000; Gunturi et al., 2000; Miura et al., 2000; Link et al., 2000; Srinivasan et al., 2000; Rae et al., 2001; MacLachlan et al., 2001; MacLachlan et al., 2002; Chen and Knowles, 2003) has been done on the plastic deformation of Ni_3Al intermetallics, both as a separate phase and as a precipitate in superalloys. As a result, the deformation mechanisms in this material are relatively well understood. A moving dislocation in the matrix phase that encounters a precipitate can either cut through the particle or climb around it. Since the intermetallic is an ordered ($L1_2$) solid solution of Al in Ni, it forms a superlattice with a perfect dislocation which is twice as large as the matrix perfect dislocation. Therefore, on entering the precipitate, a matrix dislocation causes either an anti-phase boundary (APB) or a superlattice intrinsic stacking fault (SISF), depending on the dislocation dissociation mechanism. It appears that precipitate shearing becomes an important deformation mechanism in superalloys at temperatures above 950 ^{o}C and at larger strains (latest stages of steady-state creep). At lower temperatures, considerable stresses in the range of 500 to 600 MPa are required to initiate particle shearing. Finally, also the typical anomalous yield behaviour of this intermetallic has been subject of research (Lall et al., 1979; Qin and Bassani, 1992; Vitek et al., 1996). Contrary to what is commonly observed in metals, the yield stress increases with temperature up to a peak temperature, $T_p \approx 500 - 900$ ^{o}C, and then steadily decreases. In almost any superalloy constitutive model this non-Schmid behaviour is neglected. One exception is the simple constitutive model by Allan (1995), which is specifically developed to describe these effects.

In this paper, a recently proposed crystal plasticity framework for nickel-based superalloys (Tinga et al., 2006) is extended with a precipitate phase constitutive model. The

original framework uses an efficient unit cell approach and distinguishes itself geometrically from the previously discussed superalloy unit cells (Svoboda and Lukas, 1997; Fedelich, 1999; Svoboda and Lukas, 2000; Fedelich, 2002) by the fact that special interface regions are included in the unit cell, whereby the role of the γ/γ'-interfaces is believed to play an important role in the material deformation behaviour. The material response is predicted accurately by using a non-local strain-gradient crystal plasticity model for the matrix material. In (Tinga et al., 2006) it was assumed that the γ'-precipitates remain elastic during deformation. This means that the mechanisms of recovery climb and precipitate shearing by dislocations are not considered, which limits the applicability of this model at larger plastic strains (0.5 - 2 %, depending on temperature) considerably. However, in gas turbine components local creep strains beyond these values occur, which means that the engineering practice requires a model that can be applied up to higher plastic strains.

In the present paper, a constitutive model for the precipitate phase is proposed, that describes the actual physical processes. Existing formulations for both the precipitate shearing and climb mechanisms are evaluated and combined to form an accurate constitutive description. At a number of points the existing formulations are extended to better describe the observed superalloy behaviour. Both the threshold stress for precipitate shearing and the climb velocity are made temperature dependent. On the other hand, the formulations are adapted to fit in the crystal plasticity framework proposed in (Tinga et al., 2006). The addition of a detailed precipitate constitutive model extends the application range of the framework and thus relieves the previously mentioned limitation to small plastic strains.

The model parameters are determined for the commercial turbine blade alloy CMSX-4, using experimental results from a European collaborative research project (Lecomte-Beckers et al., 2002) and additional open literature. For temperatures ranging from 750 ^{o}C to 950 ^{o}C, creep tests at different stress levels and tensile tests at different strain rates yield a consistent set of model parameters. Contrary to most of the other superalloy models, where separate sets of parameters are used for different temperature levels, the present model is shown to correctly describe the observed material behaviour for a range of conditions, using only one unique set of model parameters. Moreover, the formulation is validated by comparing model predictions to the results at other conditions than those used for the calibration.

Finally, it is shown that the observed anomalous yield behaviour and non-Schmid effects can be incorporated into the model. The extension of the crystal plasticity theory by Qin and Bassani (1992) to describe non-Schmid effects can easily be integrated in the present framework. This addition enables the model to predict the experimentally observed tension-compression asymmetry. A temperature dependent increase of the slip resistance is proposed, which incorporates the anomalous yield behaviour.

To summarize, the new and original aspects in this paper are the following:

- combination of existing formulations for the precipitate shearing and climb mechanisms and incorporation in the crystal plasticity framework proposed in (Tinga et al., 2006),
- extensions of the threshold stress for precipitate shearing and the climb velocity by adding a temperature dependence,
- description of the precipitate anomalous yield behaviour by a temperature dependent increase of the slip resistance,
- integration of the precipitate anomalous yield behaviour and other non-Schmid effects in a superalloy constitutive model,
- determination of a unique set of model parameters for the commercial alloy CMSX-4, validated in a wide range of service conditions.

In the next section the previously proposed (Tinga et al., 2006) multi-scale framework is summarized, providing definitions of the unit cell and the interaction laws. Section 3 describes the underlying strain-gradient crystal plasticity concepts and considers the internal stresses, describing the formulation of misfit and back stresses. Section 4 focuses on the constitutive models that are used, starting with the previously proposed matrix phase model. In the second part of this section the new precipitate constitutive model is proposed by describing the different deformation mechanisms and defining formulations to model the mechanical response. Also, the role of the Ni_3Al anomalous yield behaviour is discussed. In section 5, the model parameters are determined by fitting the model to experimental results on the Ni-based superalloy CMSX-4. In section 6 the model capabilities are demonstrated by comparing simulated macroscopic tensile and creep curves to experimental results for a range of temperatures, stresses and strain rates. Also the deformation of the individual regions on the microscopic level is shown and the effect of the precipitate anomalous yield behaviour on the alloy mechanical response is illustrated. Finally, section 7 forwards some concluding remarks.

2 Multi-scale framework

In this section the previously proposed (Tinga et al., 2006) multi-scale framework is summarized. First, the different length scales are illustrated, then the mesoscopic unit cell is defined, after which the scale transitions and interaction laws are described.

The different length scales covered by the model are shown schematically in Figure 2a. The *macroscopic* length scale characterises the engineering level on which a finite element (FE) model is commonly used to solve the governing equilibrium problem. The *mesoscopic* length scale represents the scale of the microstructure at the level of a macroscopic material point. At this length scale the material is considered as a compound of two different phases: γ'-precipitates embedded in a γ-matrix. Finally, the *microscopic* length scale reflects the

crystallographic nature of the individual material phases. The constitutive behaviour is defined on this level using a crystal plasticity framework.

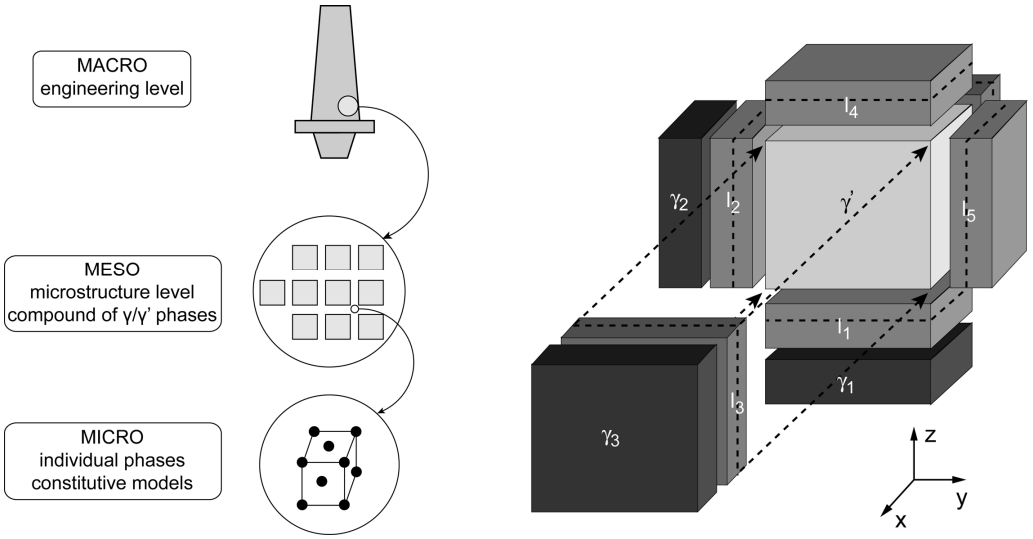

a) b)

Figure 2 Schematic overview of the model, showing (a) the multi-scale character and (b) the multi-phase unit cell, consisting of one precipitate (γ'), three matrix (γ_i) and six double interface(I_i) regions.

Considering the overall deformation level, a small strain approximation is used in the model. The intended application of the model is the analysis of gas turbine components in which deformations are small. Consequently, the initial and deformed states are geometrically nearly identical. The linear strain tensor **ε** will be used and the Cauchy stress tensor **σ** will be the appropriate stress measure.

On the material point level the Ni-based superalloy microstructure, consisting of γ'-precipitates in a γ-matrix, is represented by a unit cell containing 16 regions (see Figure 2b):

- 1 γ'-precipitate region,
- 3 γ-matrix channel regions (γ_j, j = 1… 3) with different orientations (normal along the [001], [010] and [100] direction),
- 12 interface regions (I_k^m and I_k^p, k = 1… 6) containing the γ/γ'-interfaces. A matrix and a precipitate region together form a bi-crystal, which is located on each face of the γ'-precipitate.

The interface between the two different phases plays an important role in the mechanical behaviour of the material. Therefore, special interface regions were included in the model to take into account the processes that take place at the γ/γ'-interfaces.

In the present multi-scale approach the deformation (total strain) for a certain macroscopic material point during a time increment is provided by the macro scale and the stress response is returned after the computations at the mesoscopic level. The quantities used for this macro-meso scale transition are denoted as the mesoscopic average strain ($\bar{\boldsymbol{\varepsilon}}$) and the mesoscopic average stress ($\bar{\boldsymbol{\sigma}}$). The stress tensor $\bar{\boldsymbol{\sigma}}$ is determined from the strain tensor $\bar{\boldsymbol{\varepsilon}}$ based on the specified mesoscopic configuration and the local constitutive equations of the different phases at the micro level.

The mesoscopic strain is obtained by volume averaging on their microstructural counterparts in each of the regions, defined as

$$\sum_i f^i \boldsymbol{\varepsilon}^i = \bar{\boldsymbol{\varepsilon}} \qquad i = \gamma', \gamma_1, \gamma_2, \gamma_3, \mathrm{I}_1^{\mathrm{p}}, \mathrm{I}_1^{\mathrm{m}}, \mathrm{I}_2^{\mathrm{p}}, \mathrm{I}_2^{\mathrm{m}}, \mathrm{I}_3^{\mathrm{p}}, \mathrm{I}_3^{\mathrm{m}} \tag{1}$$

where f^i are the volume fractions and $\boldsymbol{\varepsilon}^i$ the total strain tensors in the different regions. The interface regions at opposite sides of the precipitate (e.g. $\mathrm{I}_1^{\mathrm{m}}$ and $\mathrm{I}_4^{\mathrm{m}}$) are assumed to behave identically in terms of deformation, internal stress development, etc. Therefore, to the benefit of computational efficiency, only half of the interface regions is included in the equations, thereby effectively reducing the number of regions to 10.

The relation between the mesoscopic and microscopic level is provided by the constitutive models, which relate the stress tensors to the individual strain tensors for all 10 regions

$$\boldsymbol{\varepsilon}^i \quad \rightarrow \text{constitutive box} \rightarrow \quad \boldsymbol{\sigma}^i \qquad i = \gamma', \gamma_1, \gamma_2, \gamma_3, \mathrm{I}_1^{\mathrm{p}}, \mathrm{I}_1^{\mathrm{m}}, \mathrm{I}_2^{\mathrm{p}}, \mathrm{I}_2^{\mathrm{m}}, \mathrm{I}_3^{\mathrm{p}}, \mathrm{I}_3^{\mathrm{m}} \tag{2}$$

The constitutive model on the micro level, for each phase, is based on a strain-gradient enhanced crystal plasticity theory and will be described in section 4.

Inside each of the different regions, both stress and deformation are assumed to be uniform. To specify the coupling between the regions an interaction law has to be defined, where a modified Sachs approach is used for the present model: in the γ- and γ'-regions the stresses are required to be equal to the mesoscopic stress, whereas in each pair of interface regions only the *average* stress is enforced to be equal to the mesoscopic stress. This results in the following equations:

- Sachs interaction between γ'- and γ-regions:

$$\boldsymbol{\sigma}^{\gamma'} = \boldsymbol{\sigma}^{\gamma_1} = \boldsymbol{\sigma}^{\gamma_2} = \boldsymbol{\sigma}^{\gamma_3} = \bar{\boldsymbol{\sigma}} \tag{3}$$

- Modified Sachs interaction for the bi-crystal interfaces:

$$f^{\mathrm{I}_k^{\mathrm{p}}} \boldsymbol{\sigma}^{\mathrm{I}_k^{\mathrm{p}}} + f^{\mathrm{I}_k^{\mathrm{m}}} \boldsymbol{\sigma}^{\mathrm{I}_k^{\mathrm{m}}} = \left(f^{\mathrm{I}_k^{\mathrm{p}}} + f^{\mathrm{I}_k^{\mathrm{m}}} \right) \bar{\boldsymbol{\sigma}} \qquad k = 1,2,3 \tag{4}$$

Traction continuity (across the interface) and kinematical compatibility (in the plane of the interface) are added as additional requirements for the interface regions. This leads to the following supplementary equations, where $\vec{n}^k$ is the unit normal vector on the k^{th} interface:

- Compatibility between the matrix $(\mathrm{I}_k^{\mathrm{m}})$ and the precipitate side $(\mathrm{I}_k^{\mathrm{p}})$ of the k^{th} interface:

$$\boldsymbol{\varepsilon}^{\mathrm{I}_k^{\mathrm{p}}} \cdot \left(\mathbf{I} - \vec{n}^k \vec{n}^k \right) = \boldsymbol{\varepsilon}^{\mathrm{I}_k^{\mathrm{m}}} \cdot \left(\mathbf{I} - \vec{n}^k \vec{n}^k \right) \qquad k = 1,2,3 \tag{5}$$

- Traction continuity at the same interface:

$$\boldsymbol{\sigma}^{\mathrm{I}_k^{\mathrm{p}}} \cdot \vec{n}^k = \boldsymbol{\sigma}^{\mathrm{I}_k^{\mathrm{m}}} \cdot \vec{n}^k \qquad k = 1,2,3 \tag{6}$$

3 Crystal plasticity and internal stresses

A strain-gradient enhanced crystal plasticity approach (Evers et al., 2004a) is used to model the constitutive behaviour of the two phases. The next subsection gives a short description of the underlying crystal plasticity formulation. Further, the interface between the two different phases plays an important role in the mechanical behaviour of the multi-phase material, because of the development of significant internal stresses that interact with the externally applied stress. In section 3.2, the contribution of the internal stresses in the model is discussed.

3.1 Strain-gradient crystal plasticity

In a conventional crystal plasticity framework, the plastic deformation of metals naturally results from the process of crystallographic slip, which is carried by the movement of dislocations. Yet, also the hardening behaviour of metals is attributed to dislocations. Plastic deformation causes multiplication of dislocations and their mutual interaction impedes the motion of gliding dislocations, which causes strengthening. Based on their field characteristics, the total dislocation population can be considered to consist of two parts:

- statistically stored dislocations (SSD),
- geometrically necessary dislocations (GND) (Ashby, 1970).

The SSDs are randomly oriented and therefore do not have any directional effect and no net Burgers vector. They accumulate through a statistical process. On the other hand, when a gradient in the plastic deformation occurs in the material, a change of the GND density is required to maintain lattice compatibility. Individual dislocations cannot be distinguished as SSDs or GNDs. The GNDs represent therefore the fraction of the total dislocation population with a non-zero net Burgers vector. Moreover, as will be shown later, a gradient in the GND density causes an internal stress which affects the plastic deformation. These strain-gradient dependent influences give the model a non-local character.

For both phases of the considered superalloy, each with a face-centred cubic (FCC) lattice, 3 slip directions on each of the 4 octahedral slip planes can be identified, resulting in 12 equivalent slip systems. The elastic material behaviour is modelled using a standard formulation for orthotropic materials with cubic symmetry. The three independent components of the elastic tensor $^4\mathbf{C}$ of both phases in CMSX-4 at 850 $^{\mathrm{o}}$C are given in Table 1 (Busso et al., 2000a). Since no values are available at other temperatures, the temperature dependence of the

alloy (Table 2 (Lecomte-Beckers et al., 2002)) is used to scale the values for the individual phases.

Table 1 ^{4}C elastic tensor components for CMSX-4 phases at 850 ^{o}C (Busso et al., 2000a).

	γ-matrix	γ'-precipitate
C_{1111} (GPa)	190.9	216.9
C_{1122} (GPa)	127.3	144.6
C_{1212} (GPa)	100.2	112.9

Table 2 ^{4}C elastic tensor components for CMSX-4 at various temperatures (Lecomte-Beckers et al., 2002).

T (^{o}C)	C_{1111} (GPa)	C_{1122} (GPa)	C_{1212} (GPa)
20	273.6	182.4	123.7
550	239.4	159.6	121.3
700	231.4	154.3	117.6
800	223.9	149.3	114.6
850	215.4	143.6	112.1
900	207.6	138.4	111.5
950	204.4	136.3	107.9

3.2 Internal stresses

In the present model the following internal stresses are incorporated:

- misfit stress: stress that originates from the lattice misfit between the γ- and γ'-phases at the level of the coherent interface that is formed,
- back stress: stress that originates from deformation-induced plastic strain-gradients inducing a gradient in the GND density at the interfaces.

These interface effects are only included in the interface regions of the model.

Misfit

The γ- and γ'-phases both have an FCC lattice structure with a slightly different lattice (dimension) parameter. They form a coherent interface, which means that the crystal lattice planes are continuous across the interface, but a misfit strain exists to accommodate the difference in lattice parameter. The unconstrained misfit is defined as (Porter and Easterling, 1992)

$$\delta = \frac{a_{\gamma'} - a_{\gamma}}{a_{\gamma}} \tag{7}$$

with $a_{\gamma'}$ and a_{γ} the lattice parameters of the γ'- and γ-phases, respectively. The coefficients of thermal expansion ($\lambda_{\gamma'}$ and λ_{γ}) are different for both phases, which makes that the difference in

lattice parameter changes with temperature. The temperature dependence of the misfit is then given by (Link et al., 2000)

$$\delta(T) = \delta(T_r) + (\lambda_{\gamma'} - \lambda_{\gamma})(T - T_r) \tag{8}$$

where $\delta(T_r)$ is the misfit at a reference temperature T_r. Recalling that the elastic properties of γ and γ' are quite similar and supposing that the size of both phases is in the same order, it is assumed that the misfit is accommodated equally by both phases, leading to a misfit strain

$$\varepsilon_{misfit} = \frac{\frac{1}{2}(a_{\gamma'} - a_{\gamma})}{a_{\gamma}} \tag{9}$$

in the matrix (in the two directions in the plane of the interface) and the same strain with opposite sign in the precipitate. This misfit strain represents an initial elastic strain, which is constant during deformation.

Using the elastic stiffness properties of both phases and assuming that the stress perpendicular to the interface plane equals zero easily leads to the misfit stress tensor $\boldsymbol{\sigma}^{i}_{misfit}$ in both phases. Since the misfit stresses are resulting from an internal interaction between two non-fitting phases, the misfit stress is an internal stress that can be superposed to the calculated local stress (due to the externally applied load) to constitute an effective stress tensor.

Back stress

The back stress on a slip system originates from the spatial inhomogeneity of the dislocation distribution and is only related to the GND density. For SSDs, which on average have a random orientation, the back stress contribution will be negligible. The value of the back stress tensor is calculated by summation of the internal stress fields caused by the individual edge and screw dislocation densities.

$$\boldsymbol{\sigma}_{\mathbf{b}} = -\left(\boldsymbol{\sigma}_{e}^{\text{int}} + \boldsymbol{\sigma}_{s}^{\text{int}}\right) \tag{10}$$

where the minus-sign indicates its counteracting character.

For a field of edge dislocations the stress field in a point is approximated by summation of the contributions of all dislocation systems ξ in a region with radius R around that point (Bayley et al., 2006), resulting in

$$\boldsymbol{\sigma}_{e}^{\text{int}} = \frac{\mu b R^2}{8(1-\nu)} \sum_{\xi=1}^{12} \vec{\nabla} \rho_{GND}^{\xi} \cdot \left(3\vec{n}^{\xi}\vec{s}^{\xi}\vec{s}^{\xi}\vec{s}^{\xi} - \vec{s}^{\xi}\vec{s}^{\xi}\vec{n}^{\xi} - \vec{s}^{\xi}\vec{n}^{\xi}\vec{s}^{\xi} + \vec{n}^{\xi}\vec{n}^{\xi}\vec{n}^{\xi} + 4\nu\,\vec{n}^{\xi}\vec{p}^{\xi}\vec{p}^{\xi}\right) \tag{11}$$

where ρ_{GND}^{ξ} is the GND density, the vectors $\vec{s}$ and $\vec{n}$ are in the direction of the Burgers vector and the slip plane normal, respectively, b is de magnitude of the Burgers vector and $\vec{p}$ is defined as $\vec{p} = \vec{s} \times \vec{n}$, i.e. the dislocation line vector for an edge dislocation. In the original derivation of this relation for an isotropic material μ and ν are the shear modulus and the Poisson's ratio respectively. For the considered orthotropic material, the equivalent elastic constants C_{1212} and C_{1122} / (C_{1111} + C_{1122}) for the appropriate phase are used instead.

For the field of screw dislocations the stress field is given by

$$\boldsymbol{\sigma}_s^{\text{int}} = \frac{\mu b R^2}{4} \sum_{\xi=13}^{18} \vec{\nabla} \rho_{GND}^{\xi} \cdot \left(-\vec{n}^{\xi} \vec{s}^{\xi} \vec{p}^{\xi} - \vec{n}^{\xi} \vec{p}^{\xi} \vec{s}^{\xi} + \vec{p}^{\xi} \vec{s}^{\xi} \vec{n}^{\xi} + \vec{p}^{\xi} \vec{n}^{\xi} \vec{s}^{\xi} \right) \tag{12}$$

where $\vec{p} = \vec{s} \times \vec{n}$ is now perpendicular to the dislocation line direction (since the Burgers vector is parallel to the dislocation line). Note that only a non-zero gradient of the GND densities causes a non-vanishing contribution.

To calculate the back stress, it is necessary to know the distribution of the dislocation densities for all individual slip systems. These densities can be obtained from the slip gradients in the material. Since the two phases form a coherent interface this can be done on the slip system level (Evers et al., 2004b; Bayley et al., 2006). Slip gradients in the direction of the slip will be accommodated by edge dislocations and slip gradients perpendicular to the slip direction by screw dislocations. For the edge dislocations (ξ = 1… 12) the GND densities are obtained from the slip gradients $\vec{\nabla} \gamma^{\xi}$ by

$$\rho_{GND}^{\xi} = \rho_{GND,0}^{\xi} - \frac{1}{b} \vec{\nabla} \gamma^{\xi} \cdot \vec{s}^{\xi} \tag{13}$$

and for the screw dislocations (ξ = 13… 18) by

$$\rho_{GND}^{\xi} = \rho_{GND,0}^{\xi} + \frac{1}{b} \left(\vec{\nabla} \gamma^{\alpha_1} \cdot \vec{p}^{\alpha_1} + \vec{\nabla} \gamma^{\alpha_2} \cdot \vec{p}^{\alpha_2} \right) \tag{14}$$

The screw dislocation densities are the result of the combined effect of the slip gradients on the two available slip planes α_1 and α_2. An initial value $\rho_{GND,0}^{\xi}$ of the GND densities can be used to account for pre-deformation effects, if necessary.

Since the real deformation distribution in the unit cell is simplified by assuming uniform deformation inside each region, gradients in slip are captured through discrete steps in between regions only. The gradients in the dislocation density and slip, as used in the equations (11) to (14), are replaced by their piece-wise discrete analogons. Note that the Burgers vector is different in the two phases, so the choice for *b* in equations (13) and (14) is not unambiguous. However, this choice can be made arbitrarily, provided that it is done in a consistent manner. The matrix Burgers vector is selected to be used here.

4 Constitutive models

A summary of the previously proposed (Tinga et al., 2006) matrix phase constitutive model is given first. Then the newly proposed precipitate constitutive model will be elaborated.

4.1 Matrix phase

The basic ingredient of the crystal plasticity framework is the relation between the slip rates $\dot{\gamma}^{\alpha}$ and the resolved shear stresses τ^{α} for all the slip systems α. The following formulation is

used:

$$\dot{\gamma}^{\alpha} = \dot{\gamma}_0 \left\{ \frac{\left|\tau_{eff}^{\alpha}\right|}{s^{\alpha}} \right\}^{m} \left\{ 1 - \exp\left(- \frac{\left|\tau_{eff}^{\alpha}\right|}{\tau^{or}} \right) \right\}^{n} \text{sign}\left(\tau_{eff}^{\alpha}\right) \tag{15}$$

where τ^{or} denotes the Orowan stress, s^{α} the actual slip resistance and m, n and $\dot{\gamma}_0$ are material constants. The effective stress τ_{eff}^{α} on slip system α is obtained from the effective stress tensor $\boldsymbol{\sigma}_{eff}$ by

$$\tau_{eff}^{\alpha} = \boldsymbol{\sigma}_{eff} : \mathbf{P}^{\alpha} \tag{16}$$

where $\mathbf{P}^{\alpha}$ is the symmetric Schmid tensor defined as

$$\mathbf{P}^{\alpha} = \tfrac{1}{2}\left(\vec{s}^{\alpha} \vec{n}^{\alpha} + \vec{n}^{\alpha} \vec{s}^{\alpha} \right) \tag{17}$$

The unit length vectors $\vec{n}^{\alpha}$ and $\vec{s}^{\alpha}$ are the slip plane normal and slip direction, respectively. The effective stress tensor is defined as the combination of the resolved shear stress, the back stress and the misfit stress (see section 3.2) according to

$$\boldsymbol{\sigma}_{eff} = \boldsymbol{\sigma} + \boldsymbol{\sigma}_{misfit} - \boldsymbol{\sigma}_{b} \tag{18}$$

The Orowan stress, which is the stress required to bow a dislocation line into the channel between two precipitates is given by (Yuan et al., 1998) as

$$\tau^{or} = \frac{\mu b}{2\pi d} \ln\left(\frac{d}{r_0} \right) = \alpha \frac{\mu b}{d} \tag{19}$$

where the shear modulus μ is equal to the elastic constant C_{1212}, b the length of the Burgers vector, d the spacing between two precipitates (equal to the channel width) and r_0 the dislocation core radius (in the order of b). A value of $\alpha = 0.85$ was taken (Tinga et al., 2006).

The slip resistance is related to the availability of mobile dislocations and the resistance of sessile / forest dislocations and therefore depends on the total dislocation density, composed of the SSDs and the GNDs. The relation between the slip resistance and the dislocation density is defined according to

$$s^{\alpha} = c \mu b \sqrt{\left|\rho_{SSD}^{\alpha}\right| + \left|\rho_{GND}^{\alpha}\right|} \exp\left[\frac{Q}{kT} \right] \tag{20}$$

where ρ_{SSD}^{α} and ρ_{GND}^{α} are the dislocation densities, Q is the activation energy to overcome slip barriers, $k = 1.38 \times 10^{-23}$ J K^{-1} is the Boltzmann constant and T the absolute temperature.

The formulation of equation (20) requires the knowledge of all dislocation densities (12 edge dislocation densities for the SSDs and 12 edge and 6 screw dislocation densities for the GNDs). The GND densities can be obtained from the plastic deformation gradients in the material as explained in section 3.2 dealing with the back stresses. The SSD densities are calculated on the basis of an appropriate evolution equation (Evers et al., 2004a), starting from an initial value $\rho_{SSD,0}$:

$$\dot{\rho}_{SSD}^{\alpha} = \frac{1}{b}\left(\frac{1}{L^{\alpha}} - 2 y_c \rho_{SSD}^{\alpha} \right) \left| \dot{\gamma}^{\alpha} \right| \quad , \quad \rho_{SSD}^{\alpha}(t=0) = \rho_{SSD,0} \tag{21}$$

This evolution equation reflects the net effect of dislocation accumulation (left term) and annihilation (right term). The parameter y_c represents the critical annihilation length, i.e. the

average distance below which two dislocations of opposite sign annihilate spontaneously. The accumulation rate is linked to the average dislocation segment length of mobile dislocations on system α, which is determined by the current (total) dislocation state through

$$L^{\alpha} = \frac{K}{\sqrt{\left|\rho_{SSD}^{\alpha}\right| + \left|\rho_{GND}^{\alpha}\right|}} \tag{22}$$

where K is a material constant.

4.2 Precipitate phase

Ni-based superalloys contain precipitates of the $Ni_3Al(Si)$ intermetallic phase. These precipitates can deform plastically by two different mechanisms, particle shearing and climb, which are described in the next subsection. In this subsection, the anomalous yield behaviour of Ni_3Al is discussed as well. A crystal plasticity formulation for both mechanisms is proposed, properly incorporated in the slip law for the precipitate phase.

4.2.1 Precipitate deformation mechanisms

The major part of plastic deformation is accommodated by the matrix phase, where dislocations are moving through relatively narrow channels. When encountering a precipitate, a loop is created around the particle, enabling the dislocation to continue its motion on the slip plane behind the precipitate. This is illustrated in Figure 3 and, on the level of the crystal lattice, in Figure 4. The dislocation loop around the precipitate may disappear by two different mechanisms, both involving inelastic deformation of the precipitate.

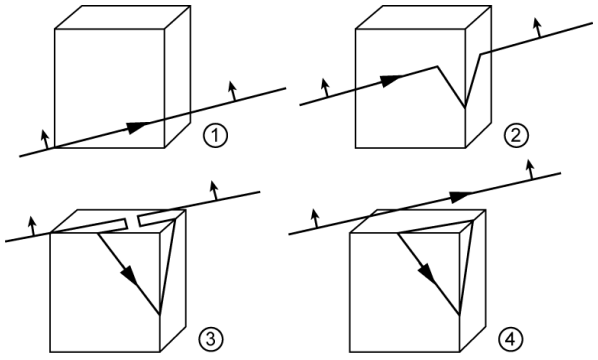

Figure 3 Illustration of a moving matrix dislocation line encountering a precipitate (1) and creating a loop around the particle (2-4).

The first mechanism is particle shearing (Figure 5), where a dislocation line moves through the precipitate. This process can occur simultaneously with the movement of the dislocation line through the matrix channels between the precipitates, or in a later stage. In the latter case a dislocation loop is initially wrapped around the particle (after the line has passed

through the matrix channels, see Figure 3) and when it shears the particle, the loop disappears. This is again a slip process along crystallographic planes.

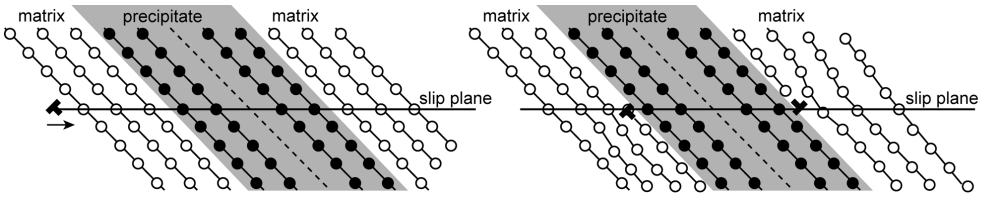

a) b)

Figure 4 Cross-sectional view of the process shown in Figure 3 on the level of the crystal lattice. a) a grown-in dislocation is moving towards the precipitate. b) the moving dislocation passed the precipitate and created a loop around the precipitate.

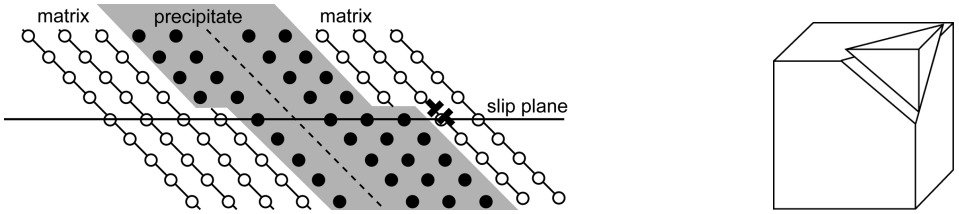

a) b)

Figure 5 a) Cross-sectional view of particle shearing. The precipitate deforms and the dislocation loop vanishes by annihilation of the positive and negative dislocation. b) The resulting deformation of the precipitate.

Since the precipitate is an ordered ($L1_2$) solid solution of Al in Ni (Ni_3Al), it forms a superlattice with a perfect dislocation (a<110>) which is twice as large as the nickel matrix perfect dislocation (½a<110>). Therefore, on entering the precipitate, a matrix dislocation causes either an anti-phase boundary (APB) or a superlattice intrinsic stacking fault (SISF), depending on the dissociation mechanism. The APB or SISF is recovered when the next matrix dislocation enters the precipitate. Therefore, in the precipitate dislocations always move in pairs, connected by an APB or SISF. This is illustrated in Figure 6 for a dislocation line that shears the precipitate without creating a loop around the particle. The respective energies determine which of the two mechanisms occurs.

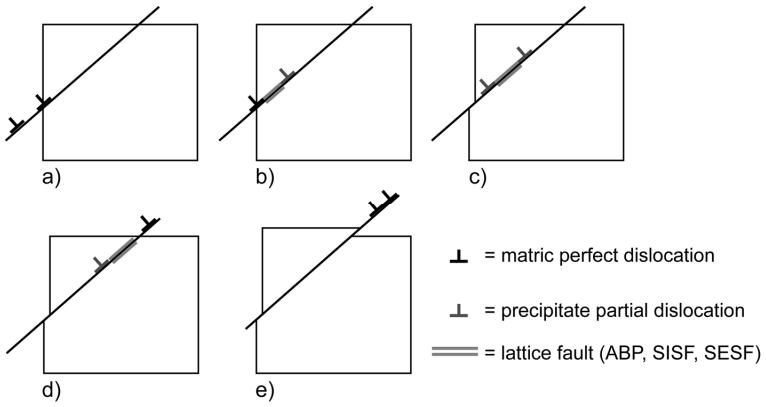

Figure 6 Schematic representation of the shearing of the precipitate superlattice by a pair of matrix dislocations.

Anomalous yield behaviour

The pair-wise movement of dislocations causes a typical phenomenon, which is known as the anomalous yield behaviour of Ni_3Al (Westbrook, 1996; Vitek et al., 1996). In experiments the following remarkable aspects are observed:

- the yield stress increases with increasing temperature up to the peak temperature (T_p),
- above T_p there is a strong strain-rate sensitivity of the flow stress, which disappears for temperatures below T_p,
- the flow stress shows a tension-compression asymmetry.

The latter two aspects cause the material to violate the Schmid law (non-Schmid behaviour). The origin of the anomalous yield behaviour is the thermally activated locking of superdislocations by cross slip, as will be explained next.

The perfect superlattice dislocations (a<110>) can dissociate in a number of ways:

1. $$a[\bar{1}01] \rightarrow \frac{a}{2}[\bar{1}01] + APB + \frac{a}{2}[\bar{1}01] \tag{23}$$

   with an APB between the superpartials. The two superpartials can further dissociate into two Shockley partials separated by a complex stacking fault (CSF)

   $$\frac{a}{2}[\bar{1}01] \rightarrow \frac{a}{6}[\bar{1}\,\bar{1}2] + CSF + \frac{a}{6}[\bar{2}11] \tag{24}$$

2. $$a[\bar{1}01] \rightarrow \frac{a}{3}[\bar{2}11] + SISF + \frac{a}{3}[\bar{1}\,\bar{1}2] \tag{25}$$

   with a SISF between the two superpartials. The energy of this dissociation is relatively high, which means that it only occurs when the APB is unstable or its energy is very high.

At low temperatures the pairs of dislocations can freely glide on the (111) planes. At higher temperatures however, screw dislocations can cross slip from (111) to (010) planes, on which they are sessile owing to the spreading of their cores onto (111) or $(1\,\bar{1}\,1)$ planes. Spreading of

the dislocation core means that two Shockley partials move away from each other (dislocation splitting), with the shear stress normal to the Burgers vector as the driving force. Before a dislocation core can spread onto another slip plane, it has to form a constriction (zero dislocation splitting) as shown in Figure 7.

Furthermore it is assumed that cross slip only occurs locally along short segments of the dislocations, leading to the formation of pinning points. These pinning points then act as obstacles to the dislocation motion. This is also known as a Kears-Wilsdorf lock. The cross slip process is thermally activated and is therefore more frequent at higher temperatures. Therefore, the density of pinning points also increases with increasing temperature, resulting in the observed increase in yield strength.

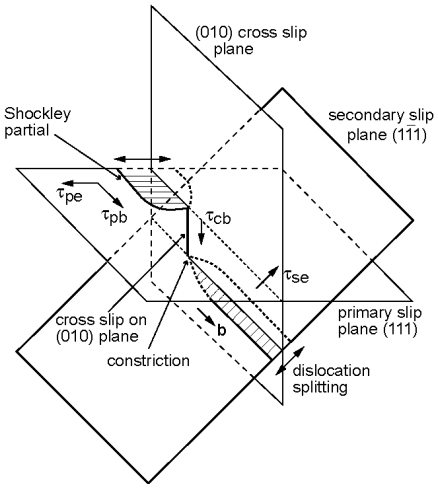

Figure 7 Schematic picture of a cross slipped screw dislocation with a core spread in a primary and secondary {111} plane, showing the shear stress components playing a role in the cross slip process.

The second mechanism of precipitate deformation is climb or recovery, where the dislocation climbs around the precipitate. This process is thermally induced and involves diffusional processes and is therefore much slower than the previous mechanism. However, the threshold is much lower, which means that it prevails when the stress is below the threshold stress for particle shearing. The mechanism is illustrated in Figure 8.

Precipitate atoms are diffusing from the one side of the precipitate to the other side along the dislocation loop (pipe diffusion). This diffusion process leads to climbing of the dislocation loop and simultaneous deformation of the precipitate. The deformation is limited to the original plane of the dislocation loop. When the dislocation loop has climbed towards the apex of the precipitate, the loop can annihilate and the deformation of the precipitate is equivalent to that caused by shearing of the particle by the matrix dislocation in its initial slip plane, as can be seen in Figure 8.

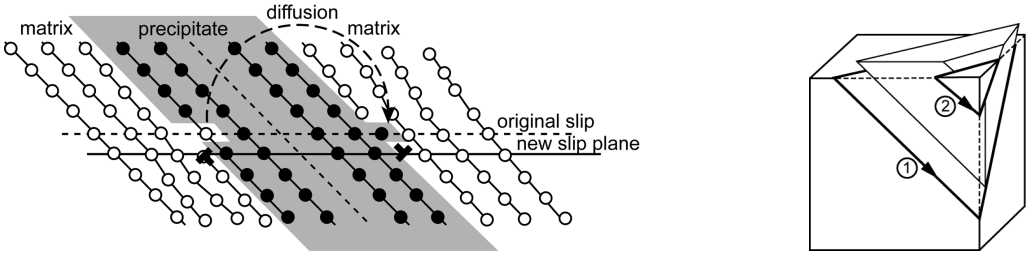

Figure 8 a) The dislocation climbs out of the slip plane, assisted by diffusion of precipitate atoms along the dislocation loop. The precipitate deforms and the loop is in a new slip plane. b) Precipitate deformation at an intermediate stage of the climb process. The loop has climbed from position 1 to position 2. When the dislocation loop has reached the apex of the precipitate, the deformation will be equal to that after shearing (see Figure 5b).

As in some other models (Svoboda and Lukas, 1997; Fedelich, 1999; Svoboda and Lukas, 2000; Fedelich, 2002), it will be assumed that precipitate deformation (by shearing or climb) only occurs when a complete loop around the precipitate is available. The precipitate deformation is therefore dependent on the matrix deformation (which generates the dislocation loops). On the other hand precipitate deformation decreases the number of deposited dislocation loops which decreases the back stress in the matrix region.

4.2.2 Crystal plasticity formulation for particle shearing

The γ'-particles do not contain grown-in dislocations (Svoboda and Lukas, 1997) like the matrix phase, so deformation of the precipitate can only occur when a matrix dislocation shears the particle. The matrix dislocation must overcome a threshold before it can enter the particle, and then the lattice slip resistance must be exceeded before it can move inside the precipitate. The magnitude of the slip rate is determined by the ratio between the effective stress and the lattice resistance, and the number of dislocations that shears the particle per unit of time. A generic equation for the slip rate, applicable to precipitate shearing, is proposed:

$$\dot{\gamma}^{\alpha} = \dot{\gamma}_0^{\alpha}\left\{1-\exp\left(-\frac{\left|\tau_{eff}^{\alpha}\right|}{s_0^{\alpha}}\right)\right\}^{p} \operatorname{sign}\left(\tau_{eff}^{\alpha}\right) \tag{26}$$

which is similar to equation (15) for the matrix phase. The effective stress on slip system α, τ_{eff}^{α}, is commonly defined through equations (16) to (18). In the matrix phase, the lattice slip resistance is strongly dependent on the dislocation density. Since no large increase in dislocation density inside the precipitate is expected, s_0^{α} is assumed to remain constant during deformation. The threshold for slip in (26) is defined as an exponential function, acting as a multiplier ranging from 0 to 1. If the effective stress is below the threshold, no slip can occur

and when the effective stress exceeds the threshold, the magnitude of the slip rate is given by the prefactor $\dot{\gamma}_0^\alpha$. The exponent p is a material constant.

The magnitude of the slip rate is governed by the number of dislocations that shears the particle per unit of time. The dislocation threshold for entering the precipitate is related to the process of dissociation into superpartials and the accompanying lattice faults (APB, SISF). This threshold is generally defined as the ratio between the lattice fault energy and the Burgers vector of the perfect superlattice dislocation. Yuan et al. (1998) and Brown and Ham (1971) present a threshold stress for particle shearing by dislocations connected by an APB which depends on the particle volume fraction. This relation shows that with increasing particle volume fraction the threshold decreases, but the origin of this dependence is not clear. Therefore, the volume fraction dependence was not included in the present model. On the other hand, no temperature dependent formulation for the threshold stress has been found in the literature, whereas experimental observations show a clear decrease of the applied stress required to initiate precipitate shearing (see section 5). Therefore, a temperature dependent threshold is proposed here

$$\tau_c^\alpha(T) = \tau_{c,0}^\alpha - a_1 \exp\left[a_2 (T - T_0)\right] \tag{27}$$

in which $\tau_{c,0}^\alpha$ is the threshold stress at a reference temperature T_0 and a_1 and a_2 are constants. The values of $\tau_{c,0}^\alpha$, T_0, a_1 and a_2 can be determined from experiments at different temperatures (section 5).

Relations for the frequency of dissociation are given in two papers by Fedelich (1999, 2002) for the SISF and APB shearing mechanisms, respectively. However, both formulations are not able to properly describe the observed behaviour of the superalloy CMSX-4. Since it is not possible to distinguish between the two mechanisms unambiguously, only the SISF mechanism is considered in the present model by modification of the relations used by Fedelich (1999). The frequency of dissociation is defined as

$$f_{diss} = f_0 \exp\left(-\frac{\Delta E}{kT}\right) \tag{28}$$

In this relation f_0 is a constant and the activation energy ΔE given by

$$\Delta E = \beta \frac{\mu^{3/2} b_{sisf}^3}{\sqrt{\left|\tau_{eff}^\alpha\right| - \tau_c^\alpha(T)}} \tag{29}$$

where μ is the precipitate shear modulus, b_{sisf} is the Burgers vector of the partial dislocation $\frac{a}{3}\langle 112\rangle$ and β is a constant. As long as the effective shear stress is below the threshold, no thermal activation is possible, $f_{diss} = 0$. For shear stresses exceeding the threshold, the frequency increases from 0 to f_0 (for $\tau_{eff}^\alpha >> \tau_c^\alpha$).

Finally the slip rate is obtained by multiplying the dissociation frequency by the number of available dislocations at the interface, the Burgers vector b and some geometric quantities:

$$\dot{\gamma}_0^\alpha = \frac{bS}{V} f_{diss} \rho_{GND,\min}^\alpha S_{\mathrm{int}} \tag{30}$$

where S and V are the particle area swept by the dislocation and the particle volume, respectively and S_{int} is the area of the interface. Note that V, S and S_{int} can be expressed in terms of the microstructural dimensions. Finally, the Burgers vector in this case is the vector used to calculate the GND density. As emphasised in the section on back stresses, this is the matrix Burgers vector.

The number of available dislocation loops can be obtained from the edge dislocation densities at the different interfaces. In general, GNDs are related to deformation gradients, but since in the current model deformation gradients are supposed to be concentrated at the interfaces between different regions (uniform strain inside regions), the GNDs represent the interface dislocations. It is assumed that only complete loops lead to precipitate deformation. A complete loop around the precipitate exists when a positive dislocation can be combined with a negative dislocation at the opposite side of the particle. However, the GND density only describes the net effect of positive and negative dislocations. Also, due to the orientation of the different slip systems relative to the particles, the slip direction $\vec{s}$ is always parallel to one of the three precipitate-matrix interfaces in the {111} slip plane, see Figure 9**.** Edge dislocations are therefore only formed at two of the three interfaces, whereas only screw dislocations are formed at the third interface and consequently the edge GND densities are zero. Taking into account these considerations, $\rho^{\alpha}_{GND,\min}$, that represents the number of available loops on the slip system α, can be obtained from the GND densities at the interfaces as

$$\rho^{\alpha}_{GND,\min} = \min\left(\left|\rho^{\alpha,I1}_{GND}\right|, \left|\rho^{\alpha,I2}_{GND}\right| \right) \tag{31}$$

where I_1 and I_2 are the two interfaces with non-zero edge GND densities, as indicated in Figure 9**.**

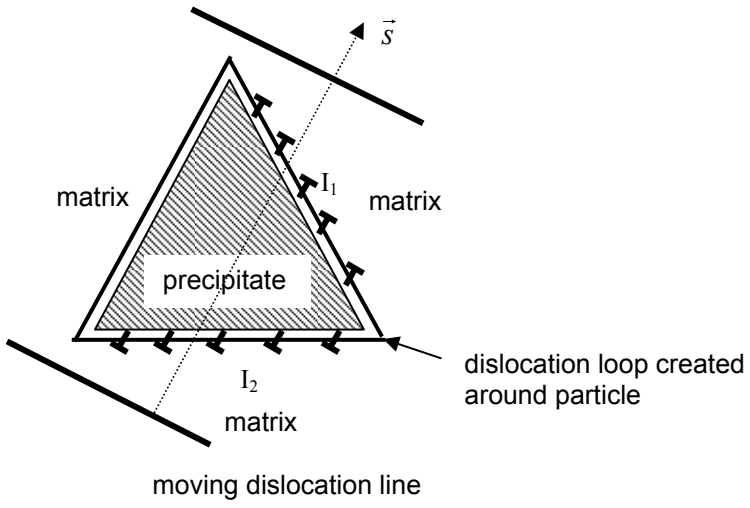

Figure 9 A dislocation line moving in a {111} plane and <011> direction is passing a precipitate. A dislocation loop is created around the particle. Edge dislocations are formed at the interfaces I_1 and I_2 only.

Finally it should be mentioned that particle shearing reduces the GND densities at the interfaces, because the deformation gradient across the interface is reduced. Since the GND densities are calculated from the slip differences between two regions, according to equation (13) and (14), this effect is automatically incorporated in the model.

Qin and Bassani (1992) extended the standard crystal plasticity theory to describe non-Schmid effects. The basic idea of their approach is that in addition to the Schmid stress (τ_{pb}, on the primary slip plane in the direction of the Burgers vector), also other stress components drive the slip behaviour. The additional stress components are (see Figure 7):

τ_{pe} : the stress on the primary slip plane normal to the Burgers vector, which drives the dislocation splitting on the primary slip plane,

τ_{se} : the stress on the secondary slip plane normal to the Burgers vector, which drives the dislocation splitting on the secondary slip plane,

τ_{cb} : the stress on the (010) cross slip plane in the direction of the Burgers vector.

These three additional stress components play a role in the cross slip process and an effective shear stress is defined as

$$\tau^{\alpha}_{non-Schmid} = \tau^{\alpha}_{pb} - A\left|\tau^{\alpha}_{pe} - \kappa\tau^{\alpha}_{se}\right| - B\,\tau^{\alpha}_{cb} \tag{32}$$

where both $\tau^{\alpha}_{pe} - \kappa\tau^{\alpha}_{se}$ and τ^{α}_{cb} decrease the effective stress due to their positive effect on the cross slip and spreading process resulting in a negative effect on the mobility. The parameter κ represents the relative importance of τ_{pe} and τ_{se} in the forming of a constriction, where the effect of both stress components is opposite: decrease of the dislocation splitting on the primary slip plane enhances formation of a constriction, and so does an increase of the splitting on the secondary slip plane. Therefore the difference of the two stress components quantifies the effect of core spreading. Finally τ_{cb} enhances the cross slip process and therefore has a negative effect on the effective stress. Note that the contribution of τ_{pb} and τ_{cb} to the generated slip simply reverses when the applied stress is reversed (from tensile to compressive), but that does not hold for the spreading mechanism governed by (τ_{pe}- $\kappa\tau_{se}$). An applied tensile stress leads to an increase of the splitting on the primary plane, which decreases the mobility and thus the (absolute value of the) effective stress, whereas a compressive stress decreases the splitting, increases the mobility and thus increases the (absolute value of the) effective stress. This tension-compression asymmetry is taken into account by the modulus operator in equation (32). The non-Schmid factors A, B and κ are material parameters which are temperature dependent. The effect can be included in the present model by replacing the external stress part of τ^{α}_{eff} in equation (16) by the right-hand part of equation (32), according to:

$$\tau^{\alpha}_{eff} = \tau^{\alpha}_{pb} - A\left|\tau^{\alpha}_{pe} - \kappa\tau^{\alpha}_{se}\right| - B\,\tau^{\alpha}_{cb} + \tau^{\alpha}_{misfit} - \tau^{\alpha}_{b} \tag{33}$$

The increase of the slip resistance with temperature due to the formation of pinning points is incorporated through a temperature dependent s_0^α :

$$s_0^\alpha = s_{0,T_p}^\alpha \exp\left(-\frac{k\left|T-T_p\right|}{D}\right) \tag{34}$$

where T_p is the peak temperature, s_{0,T_p}^α the slip resistance at T_p and D the activation energy. The decrease beyond the peak temperature is also represented by the temperature dependence of τ_c as given by equation (27). The reference temperature T_0 can thus be associated to the peak temperature T_p, which is about 750 ^{o}C for Ni_3Al (Vitek et al., 1996).

In almost any superalloy constitutive model this non-Schmid behaviour is neglected, except for the simple model proposed by Allan (1995). Experimental results and the simulations in section 6.3 show that there is a clear effect on superalloy mechanical behaviour, which justifies the inclusion of the anomalous yield behaviour in the model. However, determination of the parameters in (33) requires very specific experimental results, which may not be readily available. Only when a detailed description of the typical Ni_3Al behaviour is required, the effort to determine the parameters may be justified. In other cases the non-Schmid behaviour can be neglected by setting the constants A and B to zero, where it should be mentioned that the non-Schmid effects particularly play a role at low temperatures (well below the peak temperature).

4.2.3 Crystal plasticity formulation for climb

The generic slip rate equation for climb is again very similar to those adopted for the previous mechanisms, i.e.:

$$\dot{\gamma}^\alpha = \dot{\gamma}_0^\alpha \left\{1-\exp\left(-\frac{\left|\tau_{eff}^\alpha\right|}{\tau_{cr}^\alpha}\right)\right\} \text{sign}\left(\tau_{eff}^\alpha\right) \tag{35}$$

where the effective shear stress is again given by equations (16) to (18). While there is no distinct slip process, the lattice resistance has been replaced by a critical stress τ_{cr}^α . Furthermore the rate of the climb process is again stress and temperature driven, as will be shown later on.

There are two processes enabling a dislocation line to pass an obstacle by climb: local climb, where the dislocation segment between particles remains in the glide plane and the remainder profiles the particle surface, and general climb, where the complete dislocation climbs out of the glide plane. For materials with a low particle volume fraction, the general climb mechanism is energetically more favourable due to the smaller increase of dislocation line length. For superalloys, with a large particle volume fraction, the difference between both mechanisms is negligible and they occur with the same probability. The threshold stress for general climb is given by (McLean, 1985; Brown and Ham, 1971)

$$\tau_{cr}^\alpha = \frac{f^{\frac{3}{2}}\tau^{or}}{2^{\frac{5}{4}}} \tag{36}$$

The threshold stress is related to the Orowan stress, because the bowing of a dislocation between particles provides a stress amplification at the matrix-particle interface and thus influences the driving force for climb. The higher the Orowan stress is, the higher the threshold stress must be before the amplification effect can be used. For a high volume fraction of particles, the particle spacing is small and the dislocation line length increase for climbing around a particle is relatively high. Furthermore, in (McLean, 1985) a distinction is made between high and low stresses, but no values are specified. The threshold stresses for climb are lower than those for Orowan bowing or particle shearing, but the climb process is much slower due to the accompanying mass transfer. Therefore, the climb process only prevails if the stress is below the threshold stress for the other processes and hence the low stress threshold in (McLean, 1985) was selected.

The height of the cubic particle normal to the {111} plane is denoted $H_{\gamma'}$ and equals $\sqrt{3}$ times the precipitate cube length. The average distance for a dislocation loop to climb towards the apex of the particle is then $H_{\gamma'}/4$. The climb velocity is governed by the diffusion of precipitate atoms around the particle. This process is temperature dependent and although the dislocation loop is moving out of the slip plane, the diffusing atoms causing this climb are moving in the original slip plane. Therefore, the resolved shear stress on that slip system is considered as the driving force, as was also concluded by Fedelich (2002) from energy-based considerations. Accordingly the following relation for the climb velocity is proposed:

$$v_{climb}^{\alpha} = C\left|\tau_{eff}^{\alpha}\right|\exp\left(-\frac{Q^{c}}{R_{gas}T}\right) \tag{37}$$

where C is a proportionality constant that must be determined from experimental results. Contrary to the relation used by Fedelich, this relation contains a temperature dependence, which is derived from the underlying diffusion process. Q^c is the activation enthalpy for diffusion and R_{gas} = 8.3144 J K^{-1}mol^{-1} is the gas constant. The activation enthalpy for self-diffusion of nickel is 142 kJ/mol (Porter and Easterling, 1992). Diffusion along a dislocation line is easier than through the bulk material and the activation enthalpy is known to be reduced by a factor of 0.6 (Picu and Zhang, 2004). Therefore, a value of Q^c equal to 85 kJ/mol is used.

Finally the slip rate is obtained by dividing the climb velocity by the climb distance and multiplying by the Burgers vector, the minimum GND density and a number of geometric quantities, as was discussed in the previous section, leading to

$$\dot{\gamma}_{0}^{\alpha} = \frac{4bSv_{climb}^{\alpha}}{VH_{\gamma'}}\rho_{GND,\min}^{\alpha}S_{\text{int}} \tag{38}$$

Again V, S, $H_{\gamma'}$ and S_{int} can be expressed in terms of the microstructural dimensions. Climb also reduces the GND densities at the interfaces, because the deformation gradient across the interface is reduced.

4.2.4 Total precipitate deformation

Combining the contributions of shearing and climb (equations (26), (30), (35) and (38)) leads to the following expression for the precipitate slip rate:

$$\dot{\gamma}^{\alpha} = \frac{SbS_{\text{int}}}{V}\rho^{\alpha}_{GND,\min}\left[f_{diss}\left\{1-\exp\left(-\frac{\left|\tau^{\alpha}_{eff}\right|}{s^{\alpha}_{0}}\right)\right\}^{p} + \frac{4v^{\alpha}_{\text{climb}}}{H_{\gamma'}}\left\{1-\exp\left(-\frac{\left|\tau^{\alpha}_{eff}\right|}{\tau^{\alpha}_{cr}}\right)\right\}\right]\text{sign}\left(\tau^{\alpha}_{eff}\right) \tag{39}$$

If the stress is lower than the thresholds for particle shearing, climb still leads to precipitate deformation (but at a much lower rate). If shearing occurs, the climb contribution can be neglected. The effective resolved shear stress and temperature act as driving forces for slip in a similar way as in the γ-matrix constitutive model.

5 Model parameter determination

The presented model contains a significant number of model parameters. Therefore, a considerable amount of experimental data is required to determine the unique set of parameter values. In this section, the method that is used to determine the values for the commercial superalloy CMSX-4 is described.

An overview of the required constants and material parameters for the model and their eventual values is given in Table 3. A distinction can be made between parameters with a clear physical meaning (δ, λ_{γ}, $\lambda_{\gamma'}$, α, k, b, b_{sisf}, T_p, Q^c, R_{gas} , μ_m and μ_p) and fit parameters ($\dot{\gamma}_0$, m, n, Q, c, y_c, $\rho_{SSD,0}$, K, R, A, B, κ, D, s^{α}_{0,T_p} , p, $\tau_{c,0}$, a_1, a_2, f_0, β, C). The latter ones have to be determined from experimental data.

The CMSX-4 microstructure (Figure 1) is rather regular, so for the present model the precipitates are assumed to be cubic with a size of 500 nm. The matrix channel width is taken as 60 nm. These values yield a γ' volume fraction of 72%. Experimental results for creep tests and tensile tests on CMSX-4 are obtained from a European collaborative research project (Lecomte-Beckers et al., 2002). Additional data was collected from the open literature (Sass and Feller-Kniepmeier, 1998; Reed et al., 1999; Link et al., 2000; Gunturi et al., 2000; Schubert et al., 2000; MacLachlan et al., 2001; Knowles and Gunturi, 2002). An overview of the available tests used for the parameter determination and the model validation is given in Table 4.

A least-squares fitting procedure was used to determine the model parameters. The multi-scale model is implemented in a subroutine that calculates a tensile or creep curve for a specific condition and a set of model parameters. An optimization routine then minimizes the sum of the squared differences between the calculated results and corresponding experimental values. Using knowledge of the physical mechanisms at the microscopic level, the complete set of parameters is split-up into a number of smaller sets that can be calibrated separately.

Table 3 Model parameters for CMSX-4.

Model parameter	Symbol	Value	Unit	Used in equation
Lattice misfit at 850°C	δ	-1.1×10^{-3}		(8)
Matrix coefficient of thermal expansion	λ_γ	1.48×10^{-5}	K^{-1}	(8)
Precipitate coefficient of thermal expansion	$\lambda_{\gamma'}$	1.32×10^{-5}	K^{-1}	(8)
Reference slip rate	$\dot{\gamma}_0$	2.73×10^{-12}	s^{-1}	(15)
Rate sensitivity exponent Orowan threshold	n	3		(15)
Rate sensitivity exponent slip resistance	m	13.8		(15)
Reference activation energy	Q	3.62×10^{-20}	J	(20)
Strength parameter	c	0.034		(20)
Matrix shear modulus	μ	100.2	GPa	(20)
Matrix Burgers vector length	b	0.254	nm	(19),(20),(21)
Orowan parameter	α	0.85		(19)
Critical annihilation length	y_c	3.67	nm	(21)
Initial SSD density	$\rho_{SSD,0}$	1.0×10^{14}	m^{-2}	(21)
Dislocation segment length parameter	K	12		(22)
Radius of dislocation influence region	R	22	nm	(11),(12)
γ' lattice resistance at peak temperature	s^{α}_{0,T_p}	120	MPa	(26)
Stress exponent particle shearing	p	4		(26)
Frequency constant	f_0	4085	Hz	(28)
Energy constant	β	2.4×10^{-3}		(29)
Partial dislocation Burgers vector	b_{sisf}	0.293	nm	(29)
Precipitate shear modulus	μ_p	112.9	GPa	(29)
Threshold stress at T_p	$\tau_{c,0}$	255	MPa	(27)
Peak temperature	$T_0 = T_p$	750	°C	(27),(34)
Threshold stress temperature dependence	a_1	296	MPa	(27)
	a_2	0.0157		(27)
Non-Schmid parameters	A	0.3		(32),(33)
	B	0.1		(32),(33)
	κ	0.4		(32),(33)
Slip resistance temperature dependence	D	∞	J	(34)
Diffusion activation enthalpy	Q^c	85	kJ mol^{-1}	(37)
Climb velocity constant	C	9.4×10^{-18}		(37)

Table 4 Overview of available experimental data for the <001> orientation: for each temperature (°C) value stress (MPa) levels for the creep tests and strain rate (%/min) levels for the tensile tests are given.

Creep tests				**Tensile tests**			
750°C	**800 °C**	**850 °C**	**900 °C**	**800 °C**	**850 °C**	**950 °C**	**1000 °C**
725[a]	650	284[a]	300	0.6[a]	0.6	6.0[a]	0.6
820	750	345[a]	325	6.0[a]	6.0		4.3
		393[a]	375[a]	60[a]	60		
		650[a]	400[a]				
			425				

[a] *tests used for fitting of the model parameters*

From experimental work it is known that the mechanism of particle shearing is only active at higher stresses, since the threshold for shearing must be exceeded. A survey of experimental work on CMSX-4 (Sass and Feller-Kniepmeier, 1998; Reed et al., 1999; Gunturi et al., 2000; Svoboda and Lukas, 2000; Miura et al., 2000; Schubert et al., 2000; Link et al.,

2000; Srinivasan et al., 2000; Rae et al., 2001; MacLachlan et al., 2001; MacLachlan et al., 2002; Chen and Knowles, 2003; Prasad et al., 2005) indicates the applied stress levels, as a function of temperature, where the shearing mechanism is observed to be either active or inactive. This is represented by the two solid lines in Figure 10 and illustrates the variation of the particle shearing threshold stress with temperature. Note that in the model the threshold is defined in terms of the effective resolved shear stress, equation (29), which is a combination of the applied stress and the internal stress, whereas Figure 10 shows the externally applied (normal) stress only. For a load in the <001> direction, the Schmid factor is $\pm\frac{1}{\sqrt{6}}$ for 8 of the 12 slip systems and zero for the remaining 4 systems, resulting in a resolved shear stress equal to the applied tensile stress divided by $\sqrt{6}$. In the early stages of deformation the back stress is assumed to be negligible, so only the effect of the misfit stress has to be accounted for. The variation of the misfit stress and the effective shear stress are also plotted in Figure 10 and the latter curve was used to determine the parameters $\tau_{c,0}$ (at 750 ^{o}C), a_1 and a_2 in equation (27).

Moreover, Figure 10 can be used to determine which experiments from Table 4 must be used for fitting a specific set of parameters. For the low stress levels in the lower left part of Figure 10 the shearing mechanism is inactive and these test results are used to determine the parameters for the matrix slip and climb mechanisms. Once these parameters are known, the tests at high stress levels are used to determine the shearing parameters. The conditions used for the fitting procedure are indicated in Table 4.

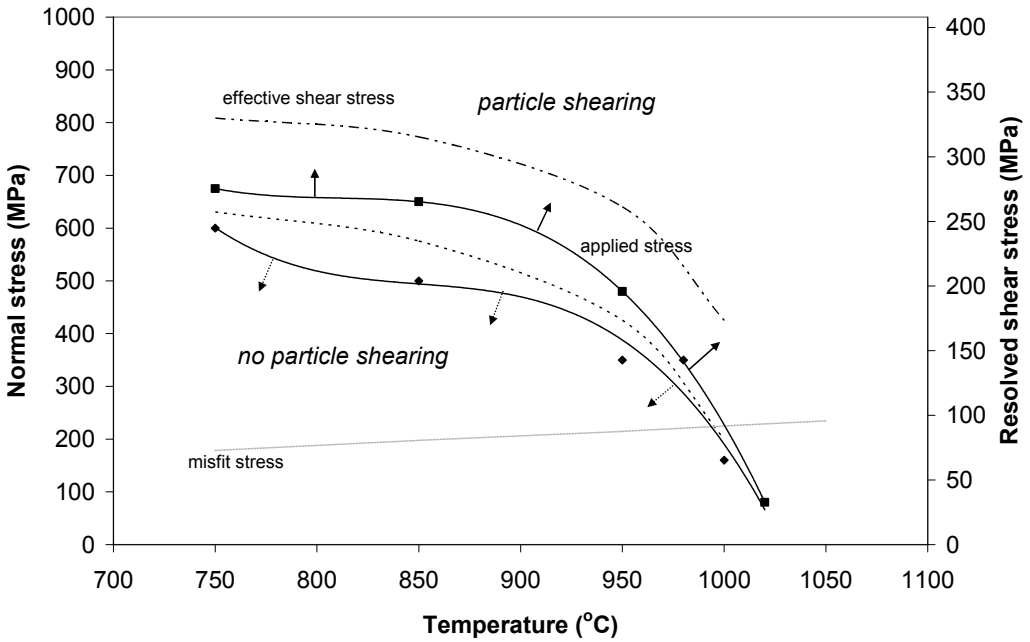

Figure 10 Activation of the precipitate shearing mechanism during creep tests as a function of stress and temperature. The solid lines are in terms of applied stress and are obtained from experimental observations. The effective stress is the sum of the applied stress and the temperature dependent misfit stress.

Climb is a very slow process, since it depends on diffusion of atoms around the precipitates. Therefore, the mechanism is not active at high strain rates during a tensile test. Further, the threshold stress for climb is related to the Orowan stress, equation (36), and has a value of 65 MPa for virgin CMSX-4. Due to the tensile misfit stresses in the precipitate, this threshold will be exceeded for any applied (tensile) stress, so the climb mechanism will be active for any condition. However, the climb mechanism cannot be separated from the matrix slip mechanism, since a certain GND density, and thus matrix slip, is required to initiate the climb mechanism. Therefore, the climb parameter C is determined simultaneously with the matrix parameters.

The matrix slip parameters $\dot{\gamma}_0$, c, y_c, $\rho_{SSD,0}$ and K are determined from the tensile and creep tests at the conditions for which the precipitate shearing is inactive. Since deformation of the matrix phase causes the development of internal stresses, which might initiate particle shearing, only the primary part of the creep curves and the part of the tensile curves up to the maximum stress level are used.

The precipitate shearing parameters p, f_0, β and s_0^α are then determined using the conditions where the shearing mechanism is active: creep tests at higher stress levels, the secondary part of the creep curves at lower stress levels and the complete tensile curves. Only a part of the complete creep curve can be used, i.e. the part up to 0.5 % (900 ^{o}C) or to 2 % (750 ^{o}C) creep strain. At higher strains or temperatures the rafting mechanism becomes active, which is not incorporated in the present model. At temperatures beyond 950 ^{o}C rafting starts right from the beginning of plastic deformation.

Finally there are a number of parameters that describe specific aspects of the material behaviour only. Determination of these parameters also requires specific experiments. The parameters that describe the non-Schmid behaviour, A, B, κ, D, T_p and s_{0,T_p}^α, can only be determined from tests that show the tension-compression asymmetry and the temperature dependence of the yield stress. Such tests are not readily available for CMSX-4, so the parameters for Ni_3Al from (Vitek et al., 1996) were used for A,B, κ and T_p and the slip resistance temperature dependence was neglected by setting the value of D to infinity, resulting in $s_0^\alpha = s_{0,T_p}^\alpha$. The parameters n and R describe the size dependence and their values can be determined from tests on specimens with different microstructural dimensions. Their values were taken from (Tinga et al., 2006).

6 Results

The model described in the previous sections has been applied to simulate the mechanical response of the single crystal Ni-based superalloy CMSX-4. Simulated creep curves and tensile curves are compared to experimental results to show that the model is able to accurately describe the material mechanical behaviour for a range of conditions. Moreover, simulation of curves for conditions not used for parameter fitting shows that the model also has predictive capabilities. Results on the micro-level are presented to illustrate that the underlying physical mechanisms are described properly by the model. Finally, the influence of non-Schmid effects in the model is demonstrated.

6.1 Simulation of creep and tensile tests

The simulated creep curves for a range of conditions are plotted in Figure 11 together with the experimental creep curves (mind the different scales along the axes). This figure shows all the cases that were used for the parameter determination.

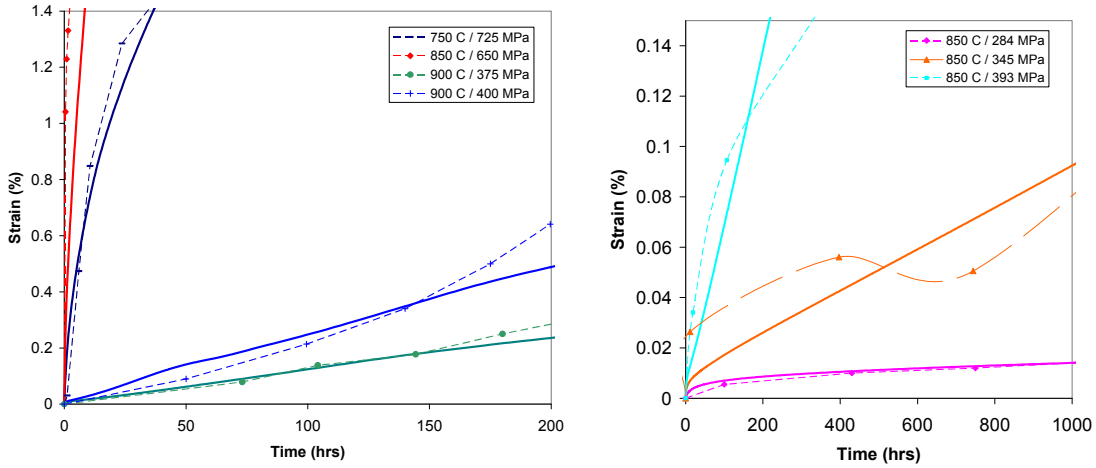

Figure 11 Simulated (solid lines) and experimental creep curves (dashed lines with markers) for the conditions that were used for parameter determination.

A wide range of temperatures and stress levels is used to determine one set of model parameters that covers all conditions. For these conditions the model simulates the real material behaviour quite well. Since the rafting process is not included in the model, it is not possible to apply the model at higher temperatures and / or longer creep times than those in Figure 11.

Figure 12 shows the comparison between simulated and experimental tensile curves for two different temperatures and several strain rates. The experiments are simulated quite well and especially the maximum and steady-state stress levels for the 800 ^{o}C curves are very close to the experimental values. The shape of the curves qualitatively matches the experiments. In general the curves show an initial peak followed by a decrease in stress, caused by the onset of

precipitate shearing, and then find their way towards the steady state stress level at which the combination of matrix and precipitate plastic flow agrees with the applied strain rate.

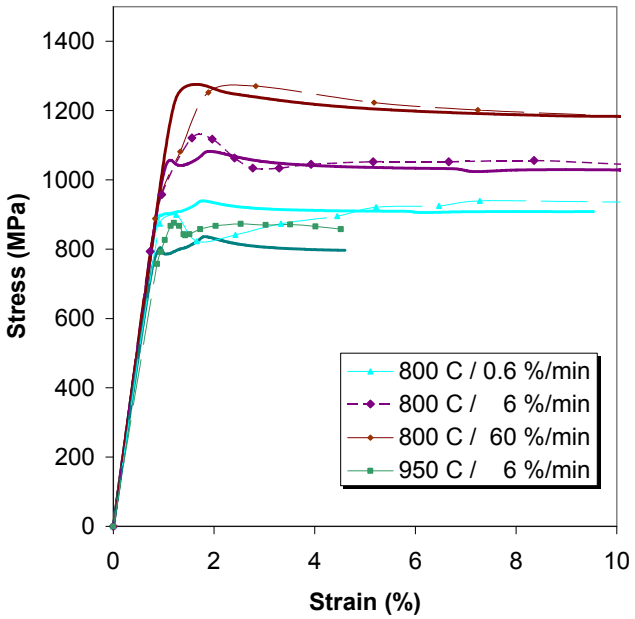

Figure 12 Simulated (solid lines) and experimental tensile curves (dashed lines with markers) for the conditions that were used for parameter determination.

Since one set of model parameters has been determined for a wide range of experimental conditions, predictions can be made for other conditions than those used for parameter determination. This is demonstrated in Figure 13, where simulated tensile test and creep experiments are compared to experimental results for various conditions. This shows that the deviations between simulation and experiments are somewhat larger than for the previous conditions, but especially the simulated tensile curves at the lower strain rates and the creep curves at 750 and 900 ^{o}C match the experiments quite adequately. The initial part of the creep curves at 800 ^{o}C is predicted well, but the transition from the primary to the secondary creep regime is not covered correctly by the model.

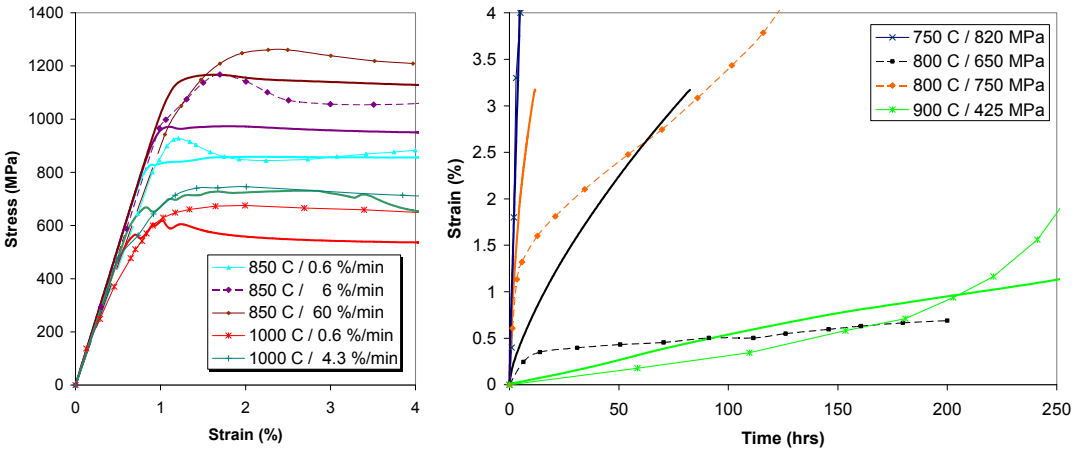

Figure 13 Simulated tensile and creep curves (solid lines) compared to experimental results (dashed lines with symbols) for several conditions.

Nevertheless, the results in this subsection show that the model is able to simulate the material behaviour quite well for a range of conditions by using only one set of model parameters. Other models are available (Fedelich, 1999; Fedelich, 2002) that may describe the behaviour for a specific loading case slightly better, since the associated set of parameters is determined specifically for that case. However, such models are generally never able to describe the material behaviour at other conditions without performing a new parameter fit procedure.

The ability to describe the material behaviour for a wide range of conditions indicates that the model contains most of the right physical mechanisms governing the material response. The main aspect that is currently still missing in the present model is the rafting mechanism, but its inclusion will be subject of future work.

6.2 Micro-level results

Figure 11, 12 and 13 in the previous subsection show the macroscopic material response, which is the weighted average behaviour of all the constituents in the multi-phase unit cell. Since in a micro-mechanical approach the processes are modelled on a microstructural level, information on the contributions of the individual regions to the overall material behaviour is available, as shown in Figure 14. In this figure, the evolution of the plastic strain in several of the unit cell regions during a tensile test is plotted together with the macroscopic stress and strain. The positions of the curves can be explained qualitatively by the differences in stress state and threshold values. Matrix region 3 and the associated interface regions are normal to the applied load, which means that the misfit stress component in the direction of the applied stress is zero. At the matrix side of interface region 1 (or 2) the misfit stress is negative and at the precipitate side it is positive. This difference in the misfit stress explains why, at the matrix side, interface 3 starts to flow earlier than interface 1, and at the precipitate side interface 1 is the first to deform

plastically. Since the misfit stresses are not considered in the matrix regions, there is no difference in effective stress level between matrix regions 1 and 3 and they therefore start to deform simultaneously. The deviation between the two curves after some deformation is caused by the difference in GND density evolution which affects the slip resistance. Finally it can be observed that the precipitate regions start to deform later than the matrix regions due to the high threshold stress of the precipitate shearing mechanism and the time required for the necessary interface dislocations to be formed.

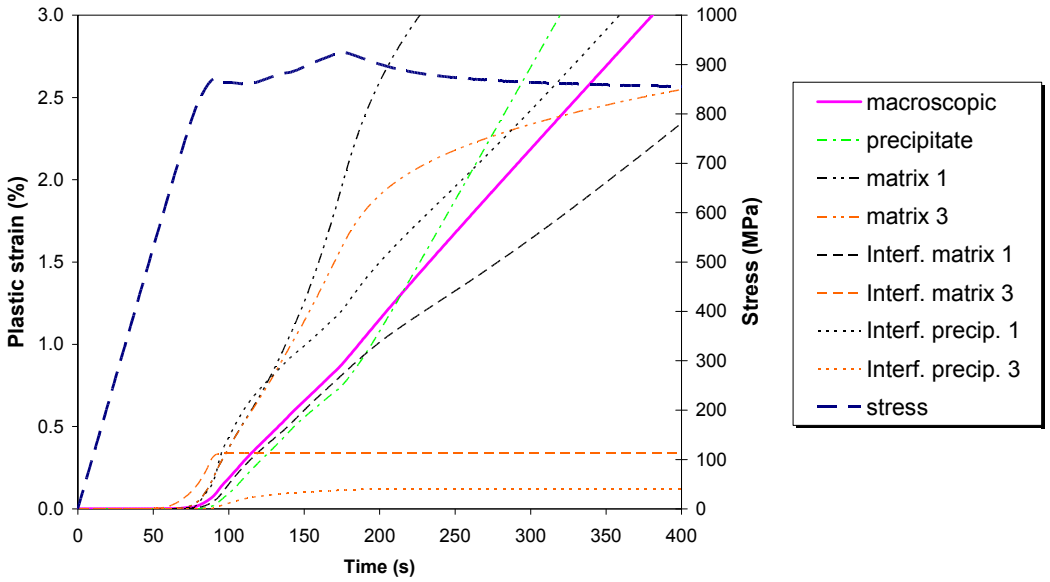

Figure 14 Plastic strain evolution in the different regions of the unit cell during a tensile test at 0.6 %/min and 800 °C. Matrix channel 1 and the associated interface regions are parallel to the applied load, channel 3 is perpendicular to the load.

The contribution of the different deformation mechanisms to the overall deformation is illustrated in Figure 15. For two creep tests under different conditions the evolution of the plastic strain due to matrix slip, precipitate shearing and recovery climb is plotted. For the first test at a low temperature and a high stress level, the matrix slip process is the main contributor to the total deformation. The shearing mechanism is also active, because the high applied stress helps to exceed the shearing threshold stress. However, the resulting plastic deformation of the precipitate leads to a decrease of the γ/γ'-misfit. Consequently the effective stress in the precipitate decreases and in combination with decreasing GND densities at the γ/γ'-interfaces this leads to a rapid decrease in precipitate shearing. The climb process, on the other hand, is a slow diffusive process with a very low stress threshold, which also depends on the available GNDs at the interfaces. This means that initially there is no climb deformation, since all GNDs

shear the precipitate. But when this mechanism stops, the climb mechanism gives a rather constant contribution to the overall deformation.

For the second case at a high temperature and a relatively low stress level the situation is quite different. The effective stress is around or below the shearing threshold, which means that precipitate shearing can hardly take place. On the other hand, the strongly temperature dependent climb process is much more active at this condition and after some time even yields the major contribution to the overall deformation.

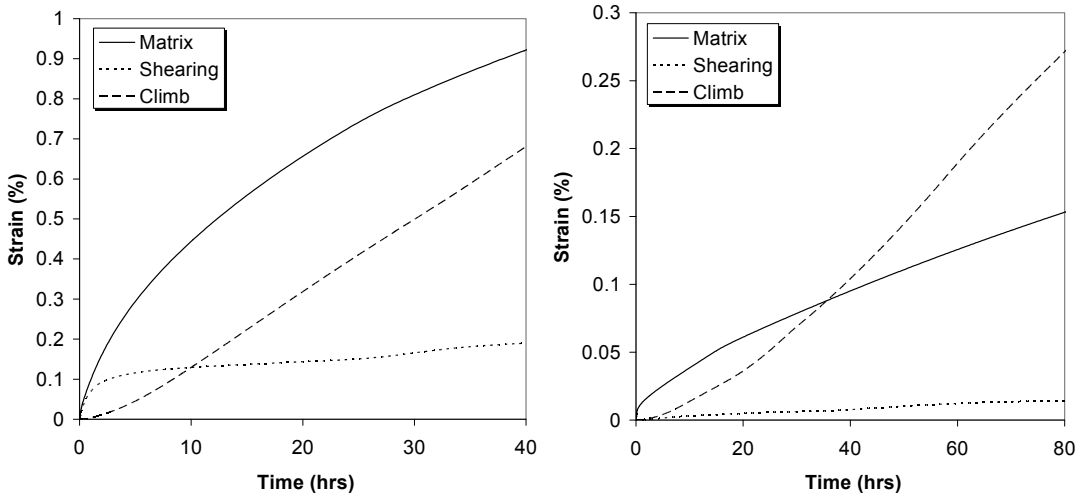

Figure 15 Contribution of the different deformation mechanisms to the total creep strain at 750 °C / 725 MPa (left) and 900 °C / 425 MPa (right).

6.3 Anomalous yield behaviour

In subsection 4.2.1 the anomalous yield behaviour of Ni_3Al was discussed. Since the superalloy is a compound of a Ni-matrix and Ni_3Al-precipitates, the anomalous yield behaviour of the precipitates will also affect the alloy mechanical behaviour. In this section the effects are discussed and illustrated.

The tension-compression asymmetry of the precipitate yield stress is introduced in the present model through equation (33). In experiments on Ni_3Al (Vitek et al., 1996) it is observed that for the <001> crystal orientation the tensile yield stress for the precipitates is higher than the compressive yield stress. The effect on the alloy response is shown in Figure 16, in which the simulated curves for opposite loads are compared to the simulation in which the non-Schmid effects are neglected ($A = B = \kappa = 0$). For a tensile load, the yielding of the precipitates starts at a higher stress, which results in a clear increase of the maximum stress level in the alloy tensile curve.

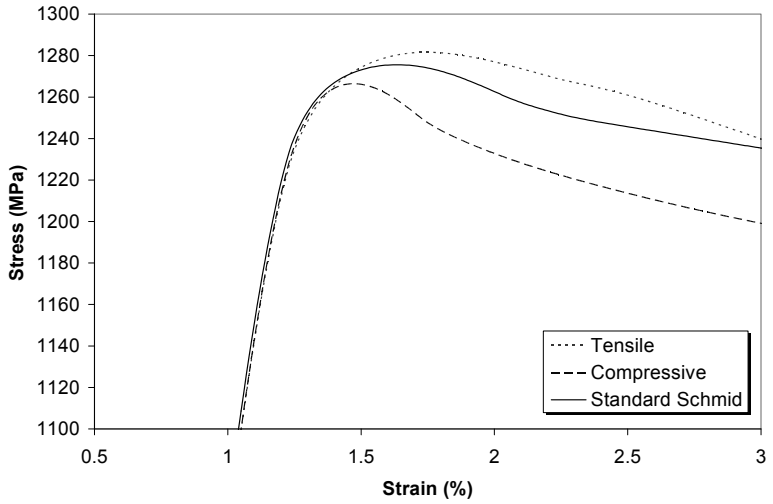

Figure 16 Effect of the precipitate tension-compression asymmetry on the alloy uniaxial loading curve at 800 °C and a strain rate of 60 %/min.

Recent numerical work on CMSX-4 by Choi et al. (2006) also showed higher stresses at tensile loading (6 %/min). However, in that work the magnitude of the tension-compression asymmetry was much smaller, because it was caused only by a geometric constraint effect imposed by the γ/γ'-microstructure. The precipitates were treated as an elastic medium and consequently the intrinsic tension-compression asymmetry of the Ni_3Al phase was neglected. Allan (1995) performed experiments on CMSX-4 at 750 °C and a strain rate of 0.6%/min, which show an effect that is even larger than in the present simulations. Also the relative position of the curves is reversed: the tensile curve is below the compressive curve (T < C). Simulations with the present model indicate that the applied strain rate has a large effect on the tension-compression asymmetry. A strain rate of 0.6%/min T < C, as was observed by Allan (1995). At a strain rate of 6 %/min T and C are almost equal, which was also observed by Choi et al. (2006), and finally a rate of 60%/min resulted in T > C (see Figure 16). This illustrates that the present model is able to qualitatively predict the observed trends in alloy tension-compression asymmetry.

The anomalous increase of the precipitate flow stress up to the peak temperature is hardly visible in the superalloy behaviour, since the initial yielding of the alloy is associated with matrix slip and not with precipitate deformation. Therefore, the precipitate slip resistance is assumed to be constant here and the normal decrease of yield stress beyond T_p is represented by the temperature dependence of the threshold stress τ_c as given by equation (27).

7 Conclusions

A detailed precipitate phase constitutive model has been added to a recently proposed crystal plasticity framework for single crystal Ni-based superalloys. Original dislocation density based formulations for the two precipitate deformation mechanisms, precipitate shearing and recovery climb, are implemented in the framework and one consistent set of model parameters for the commercial alloy CMSX-4 is determined from a database of experimental results. The model is shown to predict the material tensile response and creep behaviour for a range of temperatures and stress or strain rate levels. Also, the typical anomalous yield behaviour of Ni_3Al-intermetallics and other non-Schmid effects are implemented in the framework and the effects on the superalloy mechanical behaviour are demonstrated.

At present, the morphology of the microstructure is still assumed to remain static during deformation, which neglects the mechanism of rafting. Experimental work (Prasad et al., 2005) has shown that precipitate coarsening is completed rapidly at temperatures above 950 ^{o}C and at proportionally longer times at lower temperatures. Consequently, the assumption of a fixed morphology still limits the application region of the present model to temperatures below 950 ^{o}C , but at lower temperatures the limitation in strain level is relieved considerably. Extension of the model beyond these limitations is the subject of forthcoming work, where the detailed formulation of the precipitate deformation mechanisms as presented here will assist in the accurate modelling of the rafting process.

References

Allan, C. D., 1995. Plasticity of nickel base single crystal superalloys. Ph.D. thesis, Massachusetts Institute of Technology.

Ashby, M.F., 1970. The deformation of plastically non-homogeneous materials. Philosophical Magazine 21, 399-424.

Bayley, C.J., Brekelmans, W.A.M., Geers, M.G.D., 2006. A comparison of dislocation induced back stress formulations in strain gradient crystal plasticity. International Journal of Solids and Structures 43, 7268-7286.

Bensoussan, A., Lionis, J.L., Papanicolaou, G., 1978. Asymptotic analysis for periodic structures. North-Holland, Amsterdam.

Brown, L.M., Ham, R.K., 1971 In: Kelly, A., Nicholson, R.B. (Eds.), Strengthening Methods in Crystals. Elsevier, Amsterdam.

Busso, E.P., McClintock, F.A., 1996. A dislocation mechanics-based crystallographic model of a B2-type intermetallic alloy. International Journal of Plasticity 12 (1), 1-28.

Busso, E.P., Meissonnier, F.T., O'Dowd, N.P., 2000a. Gradient-dependent visco-plastic deformation of two-phase single crystals. Journal of the Mechanics and Physics of Solids 48 (11), 2333-2361.

Busso, E.P., O'Dowd, N.P., Dennis, R.J., 2000b. A rate dependent formulation for void growth in single crystal materials. In: Murakami, S., Ohno, N. (Eds.), 5th IUTAM symposium on creep in structures. Kluwer Academic, 41-50.

Cailletaud, G., Chaboche, J.L., Forest, S., Remy, L., 2003. On the design of single crystal turbine blades. La Revue de Metallurgie 100 (2), 165-172.

Chen, Q.Z., Knowles, D.M., 2003. Mechanism of <112>/3 slip initiation and anisotropy of γ' phase in CMSX-4 during creep at 750 C and 750 MPa. Materials Science and Engineering A 356, 352-367.

Choi, Y.S., Parthasarathy, T.A., Dimiduk, D.M., 2005. Numerical study of the flow responses and the geometric constraint effects in Ni-base two-phase single crystals using strain gradient plasticity. Materials Science and Engineering A 397, 69-83.

Choi, Y.S., Parthasarathy, T.A., Dimiduk, D.M., Uchic, M.D., 2006. Microstructural effects in modeling the flow behavior of single-crystal superalloys. Metallurgical and Materials Transactions A 37A, 545-550.

Daniel, R., Tinga, T., Henderson, M.B., 2002. Deformation modelling of the single crystal superalloy CM186LC. In: Materials for Advanced Power Engineering. COST.

Eshelby, J.D., 1957. The determination of the elastic field of an ellipsoidal inclusion, and related problems. Proceedings of the Royal Society London A 241, 376-396.

Evers, L.P., Brekelmans, W.A.M., Geers, M.G.D., 2004a. Non-local crystal plasticity model with intrinsic SSD and GND effects. Journal of the Mechanics and Physics of Solids 52, 2379-2401.

Evers, L.P., Brekelmans, W.A.M., Geers, M.G.D., 2004b. Scale dependent crystal plasticity framework with dislocation density and grain boundary effects. International Journal of Solids and Structures 41, 5209-5230.

Evers, L.P., Parks, D.M., Brekelmans, W.A.M., Geers, M.G.D., 2002. Crystal plasticity model with enhanced hardening by geometrically necessary dislocation accumulation. Journal of the Mechanics and Physics of Solids 50, 2403-2424.

Fedelich, B., 1999. A microstructure based constitutive model for the mechanical behavior at high temperatures of nickel-base single crystal superalloys. Computational Materials Science 16, 248-258.

Fedelich, B., 2002. A microstructural model for the monotonic and the cyclic mechanical behavior of single crystals of superalloys at high temperatures. International Journal of Plasticity 18, 1-49.

Ghosh, R.N., Curtis, R.V., McLean, M., 1990. Creep deformation of single crystal superalloys - modelling the crystallographic anisotropy. Acta Metallurgica et Materialia 38 (10), 1977-1992.

Gunturi, S.S.K., MacLachlan, D.W., Knowles, D.M., 2000. Anisotropic creep in CMSX-4 in orientations distant from <001>. Materials Science and Engineering A 289 (1-2), 289-298.

Hanriot, F., Cailletaud, G., Remy, L., 1991 Mechanical behaviour of a nickel-base superalloy single crystal. High Temperature Constitutive modeling - Theory and application. ASME,

Jordan, E.H., Shi, S., Walker, K.P., 1993. The viscoplastic behavior of Hastelloy-X single crystal. International Journal of Plasticity 9, 119-139.

Knowles, D.M., Gunturi, S., 2002. The role of <112>{111} slip in the asymmetric nature of creep of single crystal superalloy CMSX-4. Materials Science and Engineering A 328, 223-237.

Kouznetsova, V.G., Geers, M.G.D., Brekelmans, W.A.M., 2002. Multi-scale constitutive modelling of heterogeneous materials with a gradient-enhanced computational homogenization scheme. International Journal of Numerical Methods in Engineering 54, 1235-1260.

Kuttner, T., Wahi, R.P., 1998. Modelling of internal stress distribution and deformation behaviour in the precipitation hardened superalloy SC16. Materials Science and Engineering A 242 (1-2), 259-267.

Lall, C., Chin, S., Pope, D.P., 1979. The orientation and temperature dependence of the yield stress of Ni3(Al,Nb) single crystals. Metallurgical Transactions A 10A, 1323-1332.

Lecomte-Beckers, J., Carton, M., Schubert, F., Ennis, P.J., 2002. Materials for advanced power engineering 2002. Forschungszentrum Jülich, Jülich, Germany.

Link, T., Epishin, A., Brückner, U., Portella, P., 2000. Increase of misfit during creep of superalloys and its correlation with deformation. Acta Materialia 48, 1981-1994.

MacLachlan, D.W., Gunturi, G.S.K., Knowles, D.M., 2002. Modelling the uniaxial creep anisotropy of nickel base single crystal superalloys CMSX-4. Computational Materials Science 25, 129-141.

MacLachlan, D.W., Wright, L.W., Gunturi, G.S.K., Knowles, D.M., 2001. Constitutive modelling of anisotropic creep deformation in single crystal blade alloys SRR99 and CMSX-4. International Journal of Plasticity 17, 441-467.

McLean, M., 1985. On the threshold stress for dislocation creep in particle strengthened alloys. Acta Metallurgica 33 (4), 545-556.

Meissonnier, F.T., Busso, E.P., O'Dowd, N.P., 2001. Finite element implementation of a generalised non-local rate-dependent crystallographic formulation for finite strains. International Journal of Plasticity 17 (4), 601-640.

Michel, J.C., Moulinec, H., Suquet, P., 1999. Effective properties of composite materials with periodic microstructure: a computational approach. Computer Methods in Applied Mechanics and Engineering 172, 109-143.

Miehe, C., Schröder, J., Schotte, J., 1999. Computational homogenization analysis in finite plasticity. Simulation of texture development in polycrystalline materials. Computer Methods in Applied Mechanics and Engineering 171, 387-418.

Miura, N., Kondo, Y., Ohi, N., 2000. The influence of dislocation substructure on creep rate during accelerating creep stage of single crystal nickel-based superalloy CMSX-4. In: Pollock, T.M., Kissinger, R.D., Bowman, R.R. (Eds.), Superalloys 2000. The Minerals, Metals & Materials Society, 377-385.

Moss, S.J., Webster, G.A., Fleury, E., 1996. Creep deformation and crack growth behavior of a single crystal nickel-base superalloy. Metallurgical and Materials Transactions A 27A, 829-837.

Pan, L.-M., Shollock, B.A., McLean, M., 1997. Modelling of high-temperature mechanical behaviour of a single crystal superalloy. Proceedings of the Royal Society London A 453, 1689-1715.

Picu, R.C., Zhang, D., 2004. Atomistic study of pipe diffusion in AlMg alloys. Acta Materialia 52, 161-171.

Pollock, T.M., Argon, A.S., 1994. Directional coarsening in nickel-base single crystals with high volume fractions of coherent precipitates. Acta Metallurgica et Materialia 42, 1859-1874.

Ponte Castañeda, P., Suquet, P., 1998. Nonlinear composites. Advances in Applied Mechanics 34, 171-302.

Porter, D.A., Easterling, K.E., 1992. Phase transformations in metals and alloys. Chapman & Hall, London, UK.

Prasad, S.C., Rao, I.J., Rajagopal, K.R., 2005. A continuum model for the creep of single crystal nickel-base superalloys. Acta Materialia 53, 669-679.

Qin, Q., Bassani, J.L., 1992. Non-Schmid yield behavior in single crystals. Journal of the Mechanics and Physics of Solids 40 (4), 813-833.

Rae, C.M.F., Matan, N., Reed, R.C., 2001. The role of stacking fault shear in the primary creep of [001]-oriented single crystal superalloys at 750 C and 750 MPa. Materials Science and Engineering A 300, 125-134.

Reed, R.C., Matan, N., Cox, D.C., Rist, M.A., Rae, C.M.F., 1999. Creep of CMSX-4 superalloy single crystals: effects of rafting at high temperature. Acta Materialia 47 (12), 3367-3381.

Rist, M.A., Oddy, A.S., Reed, R.C., 2000. Three-dimensional simulation of inhomogeneous tertiary creep in single-crystal superalloy test pieces. Scripta Materialia 43, 719-725.

Sanchez-Palencia, E., 1980. Non-homogeneous media and vibration theory, Lecture notes in physics 127. Springer, Berlin.

Sass, V., Feller-Kniepmeier, M., 1998. Orientation dependence of dislocation structures and deformation mechanisms in creep deformed CMSX-4 single crystals. Materials Science and Engineering A 245, 19-28.

Schubert, F., Fleury, G., Steinhaus, T., 2000. Modelling of the mechanical behaviour of the single-crystal turbine alloy CMSX-4 during thermomechanical loading. Modelling and Simulation in Materials Science and Engineering 8, 947-957.

Shenoy, M.M., Gordon, A.P., McDowell, D.L., Neu, R.W., 2005. Thermomechanical fatigue behavior of a directionally solidified Ni-base superalloy. Journal of Engineering Materials and Technology 127, 325-336.

Srinivasan, R., Eggeler, G., Mills, M.J., 2000. γ'-cutting as rate-controlling recovery process during high-temperature and low-stress creep of superalloy single crystals. Acta Materialia 48, 4867-4878.

Svoboda, J., Lukas, P., 1997. Modelling of recovery controlled creep in nickel-base superalloy single crystals. Acta Materialia 45 (1), 125-135.

Svoboda, J., Lukas, P., 2000. Creep deformation modelling of superalloy single crystals. Acta Materialia 48 (10), 2519-2528.

Tinga, T., Brekelmans, W.A.M., Geers, M.G.D., 2006. Strain-gradient crystal plasticity based modelling of single crystal nickel-based superalloys. International Journal of Solids and Structures submitted, 1-30.

Vitek, V., Pope, D.P., Bassani, J.L., 1996 Anomalous yield behaviour of compounds with L12 structure. In: Nabarro, F.R.N., Duesbery, M.S. (Eds.), Dislocations in solids. Volume 10: L12 ordered alloys. Elsevier, Amsterdam.

Westbrook, J.H., 1996 Superalloys (Ni-base) and dislocations - An introduction. In: Nabarro, F.R.N., Duesbery, M.S. (Eds.), Dislocations in solids. Volume 10: $L1_{2\ \text{ordered alloys}}$. Elsevier, Amsterdam.

Willis, J.R., 1981. Variational and related methods for the overall properties of composites. Advances in Applied Mechanics 21, 1-78.

Yuan, C., Guo, J.T., Yang, H.C., 1998. Deformation mechanism for high temperature creep of a directionally solidified nickel-base superalloy. Scripta Materialia 39 (7), 991-997.

Yue, Z., Lu, Z., 1998. Self-consistent constitutive modeling of the creep behaviour of nickel-base directionally solidified superalloys with different grain orientations. Journal of Material Science and Technology 14, 15-19.

Yue, Z.F., Lu, Z.Z., Zheng, C.Q., 1996. Evaluation of creep damage behavior of nickel-base directionally solidified superalloys with different crystallographic orientations. Theoretical and Applied Fracture Mechanics 25 (2), 127-138.